



# Synergistic effect in MMT-dispersed Au/TiO<sub>2</sub> monolithic nanocatalyst for plasmon-absorption and metallic interband transitions dynamic CO<sub>2</sub> photo-reduction to CO



Muhammad Tahir <sup>a,b,\*</sup>

<sup>a</sup> Chemical Reaction Engineering Group (CREG), Department of Chemical Engineering, Faculty of Chemical and Energy Engineering, Universiti Teknologi Malaysia (UTM), 81310 UTM, Johor Bahru, Johor, Malaysia

<sup>b</sup> Department of Chemical Engineering, COMSATS Institute of Information Technology, Lahore, Pakistan

## ARTICLE INFO

### Article history:

Received 1 April 2017

Received in revised form 14 July 2017

Accepted 23 July 2017

Available online 24 July 2017

### Keywords:

CO<sub>2</sub> Photo-reduction

Inter-band transition

Plasmon absorption

Synergistic effect

Montmorillonite

Monolithic support

## ABSTRACT

Structured montmorillonite (MMT) dispersed Au/TiO<sub>2</sub> nanocomposite has been designed and synthesized through a facile sol-gel method. Cordierite monolithic support was employed in order to load the catalyst for improved photo-activity and reusability in CO<sub>2</sub> utilization process. The samples were characterized by XRD, Raman, SEM, TEM, FTIR, XPS, N<sub>2</sub> adsorption-desorption, UV-vis and PL spectroscopy. The synergistic effect of MMT-dispersed Au/TiO<sub>2</sub> nanocatalyst was evaluated in a gas-phase dynamic monolith photoreactor system using UV and visible light irradiations. The maximum CO yield over 0.5 wt.% Au–10 wt.% MMT-loaded TiO<sub>2</sub> catalyst reached to 1223 μ mole g-catal. <sup>-1</sup> h<sup>-1</sup>, a 24 fold higher than the amount of CO produced over the 10 wt.% MMT/TiO<sub>2</sub> and 68 times the amount of CO produced over the bare TiO<sub>2</sub> catalyst. The other products observed with considerable amounts were CH<sub>4</sub> and C<sub>2</sub>H<sub>6</sub>. This enactment under UV-light was due to interband transition of Au in catalyst composite. Enhanced photo-activity under simulated solar energy for CO<sub>2</sub>-to-CO reduction was due to LSPR effect of Au in the MMT/TiO<sub>2</sub> sample. More importantly, the performance of Au-MM/TiO<sub>2</sub> catalyst for CO evolution under UV-light was 6 folds higher than using visible light. The synergistic effect between MMT transition metals and Au ions and faster adsorption-desorption process contributed to remarkably enhance dynamic CO<sub>2</sub> reduction to CO. The present design of catalyst provides prolonged stability to catalyst while CO evolution sustained even after 44 h of operation time. The reaction mechanism developed to understand the role of Au/MMT and monolithic support on the photo-activity and reusability of catalyst for CO<sub>2</sub> photo-reduction to fuels.

© 2017 Elsevier B.V. All rights reserved.

## 1. Introduction

Solving greenhouse gas CO<sub>2</sub> problem requires technologies for its potential conversion to fuels with reduced emissions, less waste and cost effective [1]. Since CO<sub>2</sub> is a rather inert and stable molecule, thus its reduction is a challenging task because of involving higher input energy [2]. Therefore, photocatalytic conversion of aqueous CO<sub>2</sub> into useful fuels such as CH<sub>3</sub>OH [3], CH<sub>4</sub> [4] and CO [5] by the use of light irradiation is of great interest, an attractive approach and cost-effective process. Among the semiconductors, most widely photo-catalysts tested in CO<sub>2</sub> reduction applications include ZnO [6], CdS [7], TiO<sub>2</sub> [8], WO<sub>3</sub> [9] and g-C<sub>3</sub>N<sub>4</sub> [10]. However, TiO<sub>2</sub> prevailed in recent years due to its rewards such as

available at low cost, thermal stability, resistance to chemicals and high oxidative potential [11,12]. Conversely, it does not absorb visible light, while poor photo-activity is a great challenge due to fast charge carrier recombination rate. One prospective path to enhance TiO<sub>2</sub> activity is by its dispersion into clay micro-sheets. Recently, natural clay minerals as inorganic support are considered low-cost and environmental friendly to develop clean technology for various applications. TiO<sub>2</sub> can be dispersed in suitable matrix of these green clay materials to develop clay-TiO<sub>2</sub> hetero-junction [13]. The multiple benefits of clay support include green materials with low cost, safer for the environment and efficient for CO<sub>2</sub> adsorption [14].

Among the natural clays, montmorillonite (MMT) is a pillared clay with great potential as a support for adsorption applications due to favorable microporous structure, high cations exchange capacity and superior charge trapping ability [15]. MMT structure is suitable to develop hetero-junction by dispersing TiO<sub>2</sub> on the MMT surface or within the MMT interlayers and galleries [16]. Previously, CdS nanoparticles deposited on MMT for photocatalytic CO<sub>2</sub>

\* Corresponding author at: Department of Chemical Engineering, COMSATS Institute of Information Technology, Lahore, Pakistan.

E-mail addresses: [mtahir@cheme.utm.my](mailto:mtahir@cheme.utm.my), [bttahir@yahoo.com](mailto:bttahir@yahoo.com)

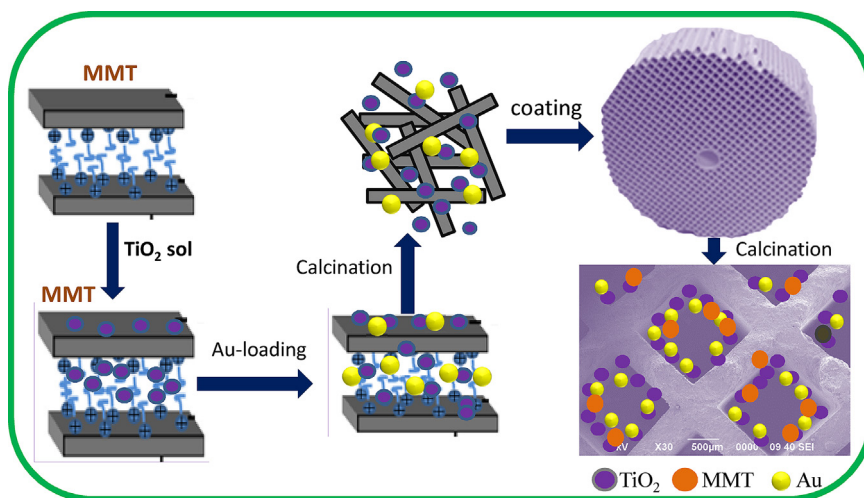


**Fig. 1.** Scheme for the sol-gel preparation of MMT-dispersed Au/TiO<sub>2</sub> catalyst coated over monolithic support.

reduction to CO, CH<sub>4</sub> and H<sub>2</sub> under UV-light irradiation has been investigated [17]. Koci et al. [18] reported photocatalytic CO<sub>2</sub> reduction by H<sub>2</sub>O to CO, CH<sub>4</sub> and H<sub>2</sub> using ZnS/MMT nanocomposite. We successfully demonstrated selective and enhanced photoactivity of MMT/TiO<sub>2</sub> nanocomposite for CO<sub>2</sub> photo-reduction with H<sub>2</sub>O to CH<sub>4</sub> [19,20] and CO<sub>2</sub> reduction with CH<sub>4</sub> to CO and hydrocarbons [21]. The photocatalytic activity of MMT/TiO<sub>2</sub> nanocomposite can be further improved by loading suitable metals and non-metals ions. Among the metals, copper, silver, gold, nickel and platinum have resulted in increased yields and selectivity [22–26].

Noble metals combined with semiconductors have been extensively explored for hindered charges recombination rate under UV-light irradiation and Plasmon-induced activity under visible light irradiation. Ag-loaded TiO<sub>2</sub> was investigated with enhanced photoactivity and selectivity for photocatalytic CO<sub>2</sub> reduction to CO and CH<sub>4</sub> under UV and visible light irradiations [27,28]. Similarly, Au-In-loaded TiO<sub>2</sub> co-catalysts investigated for selective CO<sub>2</sub> reduction to CO under UV-light irradiations [29]. Previously, many researchers have reported Plasmon-enhanced activity of TiO<sub>2</sub> in the presence of Au, Ag and Cu metals for photo-induced CO<sub>2</sub> reduction to solar fuels under visible light irradiations [30–33]. Noble metals alone can absorb UV-light irradiation to perform as a photo-catalyst through interband transition. Au-NPs themselves also contribute to the photo-activity under UV-light, yet photo-activity may not be significant. However, by loading Au-NPs over the TiO<sub>2</sub>, photo-activity can be enhanced significantly, due to Au-NPs metallic interband electron transition [34]. Additionally, optical properties of Au-NPs are strongly affected by their size and shape. Large size Au-NPs could enhance TiO<sub>2</sub> photo-activity through LSPR effect or through metallic interband transition, thus ability to absorb light in a broad wavelength range. Instead, Au-NPs also prevent charges recombination rate and could transfer electrons from the semiconductor towards CO<sub>2</sub> for its reduction. This synergistic effect of Au-NPs is beneficial for higher level of photoactivity for enhanced CO<sub>2</sub> reduction [35–38]. Thus, it is imperative to use Au-NPs for the modification of MMT/TiO<sub>2</sub> composite to explore further for photocatalytic CO<sub>2</sub> reduction applications.

On the other hand, photo-catalysis process is considered efficient only if there is effective interaction between the light irradiations, catalyst and reactants. To date, slurry and cell type photo-reactors have been widely explored in which catalysts are used as a suspension or distributed over the reactor surface [39–41]. The slurry type reactors have limitations such as poor light utilization efficiency due to less exposed active surface area, the loss of catalyst during recycling, high cost of photo-catalyst separation

from the slurry system, and lower intensity to stimulate complex nature of photocatalytic reaction [42]. Therefore, the design of highly efficient photo-reactors for CO<sub>2</sub> reduction is crucial to scale up photo-technology from the laboratory to commercial level. Currently, immobilized photocatalytic systems with enhanced light utilization efficiency have attracted much attentions [43]. Among the different supports, monolithic substrates are mainly studied because of their unique structure and large photonic efficiency [44,45]. In this perspective, monolithic support found very efficient for photocatalytic CO<sub>2</sub> reduction to CO with enhanced selectivity and yield [46,47]. In the recent literature, application of Au-promoted TiO<sub>2</sub>/MMT nanocomposite loaded over the monolithic support for CO<sub>2</sub> reduction by H<sub>2</sub> to CO has never been reported. In this context, further research involving MMT supported Au/TiO<sub>2</sub> photo-catalyst for gas phase CO<sub>2</sub> conversion in a continuous monolith photo-reactor to produce renewable fuels is warranted.

In this study, we designed and synthesized MMT dispersed Au/TiO<sub>2</sub> nanocomposite immobilized onto monolithic support for selective and enhanced photo-induced CO<sub>2</sub> reduction to CO under UV-light irradiation through metallic interband transition. Performance of composite catalyst was further investigated under simulated solar energy via LSPR effect of Au-NPs. The nanocatalysts synthesized by a facile sol-gel method were dip-coated over the cordierite support. For systematic understanding synergistic effect of support and catalyst, in conjunction with metallic interband transition and Plasmon absorption, photo-catalytic reaction mechanism is critically discussed. Stability analysis of nanocomposite was conducted to evaluate the life and reusability of the catalyst for dynamic photocatalytic CO<sub>2</sub> reduction applications.

## 2. Experimental

### 2.1. Catalyst preparation

Commercially available tetra-isopropyl orthotitanate (98%, Merck), montmorillonite (1.4 P, Sigma-Aldrich) and AuCl<sub>3</sub> (Sigma-Aldrich) were used without further purification. Structured MMT dispersed Au-loaded TiO<sub>2</sub> nanocomposites were synthesized through a facile single step sol-gel method. Typically, 20 mL titanium solution dispersed in 45 mL isopropanol was taken into flask for the hydrolysis process. The solution was hydrolysed by adding 15 mL acetic acid (1 M) under continuous stirring. Next, fixed quantity of MMT-clay was dispersed in isopropanol by stirring 1 h, then added into titanium solution. After stirring for 6 h, the appropriate quantity of AuCl<sub>3</sub> dissolved in isopropanol was added to above

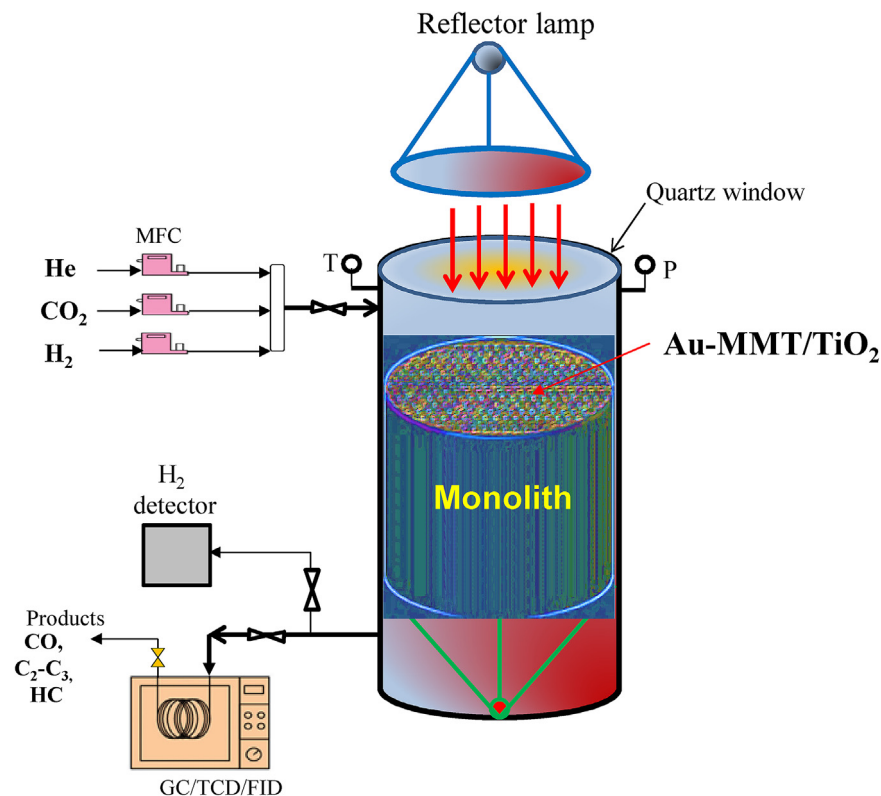


**Fig. 2.** Experimental set-up of monolith photo-reactor for dynamic photocatalytic  $\text{CO}_2$  reduction by hydrogen to fuels using reflector lamp.

solution and stirred the mixture for another 6 h to complete the intercalation process. Finally, clear thick titanium sol was transferred into glass container for coating over the monolith substrate.

The monolith used were cordierite in structure with channels per square inch (CPSI) 200, 6 cm diameter and 2 cm length. The monolithic supports were purchased from Pingxiang Meitao Company, China. After washing with water and acetone, to remove impurities, all the monoliths were dried at 110 °C and finally initial weights were calculated. To ensure the accuracy of the results, three reading were recorded for the bare and coated monoliths, the resultant was catalyst weight loaded over the channels. For catalyst coating, weighed monoliths were dipped for 10 s, then removed off, while blown off with hot compressed air to get fine catalyst layer over the channels surface. The amount of catalyst loading could be increased by repeating the same procedure. Finally, catalyst coated monoliths were put in the oven and dried at 110 °C for 12 h before calcining at a temperature of 500 °C for 5 h. The schematic presentation of MMT dispersed  $\text{TiO}_2$  catalyst coating over the monolithic support is depicted in Fig. 1.

## 2.2. Catalyst characterization

X-ray Diffraction (XRD) analysis of the samples was conducted using a Bruker D8 advance diffractometer equipped with  $\text{Cu-K}\alpha$  radiation ( $\lambda = 0.154 \text{ nm}$ ). The data was obtained at 40 kV and 40 mA in the scan range of  $10^\circ \leq 2\theta \leq 80^\circ$ , 1.2° per min scan speed, and 0.02° step size. The cordierite structure of monolith was inspected using Scanning Electron Microscopy (SEM) with JEOL JSM6390 LV SEM. The morphology of the materials was examined using field emission scanning electron microscopy (FESEM) using Hitachi SU8020 instrument with double condenser optics to ensure full control of probe current from 1 pA to more than 5 nA. Energy-dispersive X-ray spectroscopy (EDX) mapping analysis was conducted to find out elements composition and distribution inside

the composite sample. The High Resolution Transmission Electron Microscopy (HR-TEM) analysis was conducted using FEI-Tecni G<sub>2</sub> to obtain mesoporous and lattice structure in a composite sample.  $\text{N}_2$  adsorption-desorption isotherms were obtained at –196 °C using Micrometric ASAP 2020 analyser before degasified at 250 °C for 4 h. The X-ray photo-electron spectroscopy (XPS) was conducted with Omicron DAR-400 analyser. The survey spectra recorded in the range of 0–1400 eV and peaks binding energies were calibrated using C1s (284.60 eV) signal as the internal standard. Fourier Transformed Infrared (FT-IR) Spectrometer peaks were obtained in the range of 400–4000  $\text{cm}^{-1}$  employing Spectrum 2000 Explorer Spectrometer. Diffuse reflectance spectra (DRS) of the powder samples were collected by employing Agilent, Cary 100 UV-vis spectrophotometer, equipped with integrated sphere assembly for powder samples analysis. Raman and photoluminescence (PL) spectra of samples were recorded on Xplora Plus Spectrophotometer (HORIBA Scientific) with a 532 nm and 325 nm emitting lasers as an excitation sources, respectively.

## 2.3. Photocatalytic activity test

The photo-catalytic  $\text{CO}_2$  reduction to CO by hydrogen was tested in a gas phase continuous flow photo-reactor as depicted in Fig. 2. The reactor consists of cylindrical vessel having 150  $\text{cm}^3$  total volume and a quartz glass window of thickness 8 mm used for passing light irradiations. A 200 W Hg reflector lamp was used as a source of UV-light irradiations, located at the top of the reactor and cooling fans were employed to remove lamp heat. The light intensity of 150  $\text{mW cm}^{-2}$  at wavelength 252 nm was measured with an online optical process monitor ILT OPM-1D and a SED008/W sensor. The source of visible light irradiation was a simulated sunlight using a solar simulator LCS-100 (Newport) integrated with UV-cut filters with light intensity equal to one solar spectrum (100  $\text{mW/cm}^2$ ). The gasses feed rates were controlled using online mass flow con-

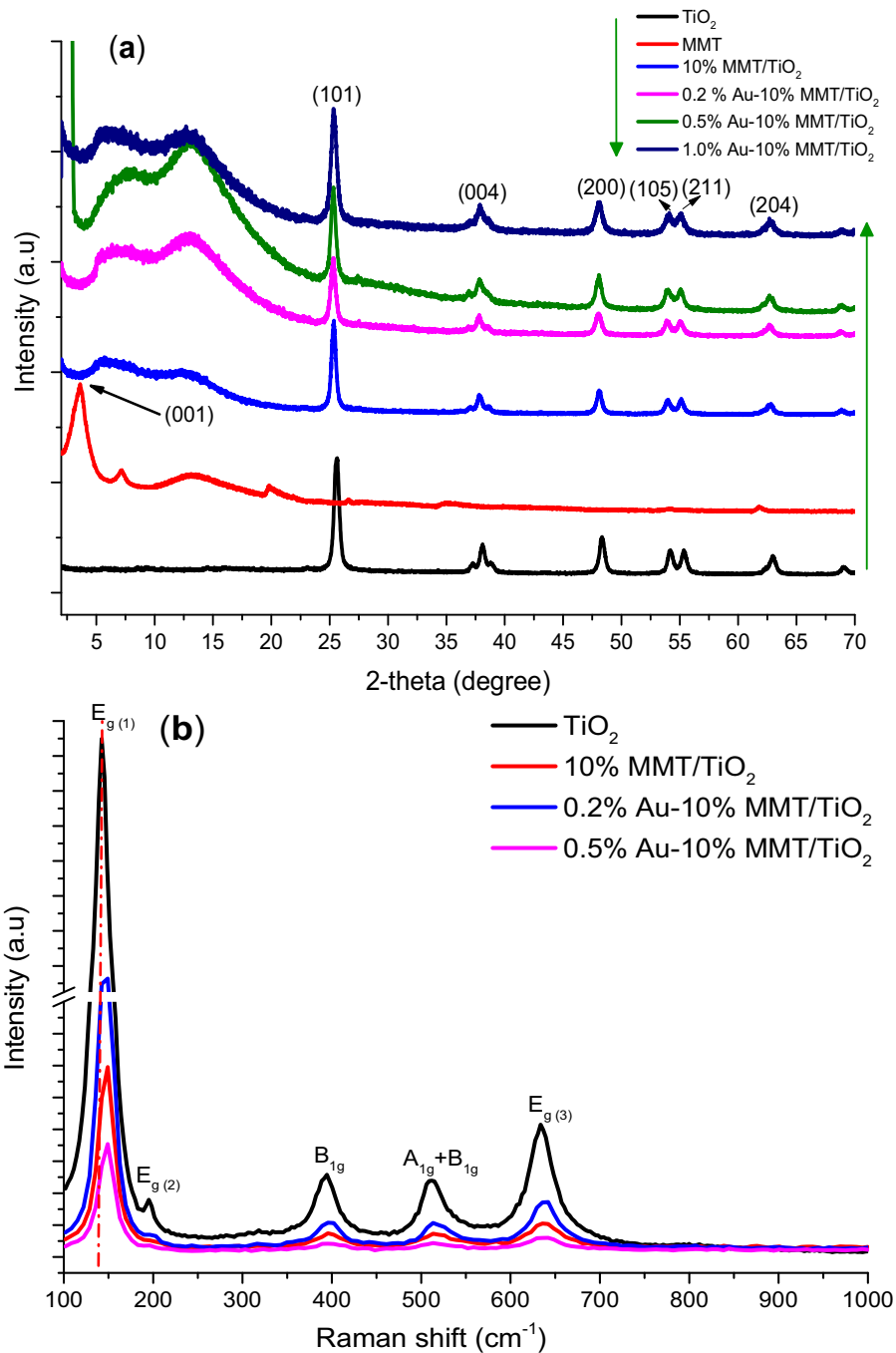


**Fig. 3.** (a) X-ray diffraction patterns of  $\text{TiO}_2$ , MMT and Au-MMT/ $\text{TiO}_2$  catalysts; (b) Raman analysis of  $\text{TiO}_2$ , MMT/ $\text{TiO}_2$  and Au-doped MMT/ $\text{TiO}_2$  samples.

trollers (MFC). A gas mixture was used to ensure all the gases were uniformly mixed before entering into the reactor. The temperature of the reactor was controlled using temperature controller while pressure was measured using pressure gauge.

The catalyst coated ceramic monoliths with channel per square inch (CPSI) 200 were inserted inside the stainless steel chamber. Before starting the experiment, the reactor was purged with feed gas mixture ( $\text{CO}_2$  and  $\text{H}_2$ , purity = 99.99%) flowing continuously at total flow rate 20 mL/min. The feed mixture ( $\text{CO}_2/\text{H}_2$ ) molar feed ratio of 1.0 was fixed while flow rates of 10 mL/min was adjusted for each gas with a space velocity of  $0.13 \text{ s}^{-1}$ . Continuous flow mode was used in all the experiments conducted at 100 °C and atmospheric pressure. Gas chromatograph (GC-Agilent Technologies 6890 N, USA) equipped with TCD detector and a FID

detector was used for the products analysis. Besides, HP-PLOT Q capillary column (Agilent, length 30 m, ID 0.53 mm, film 40  $\mu\text{m}$ ) was connected with FID detector while Porapak Q and Mol Sieve 5A columns were connected to TCD detector.

### 3. Results and discussion

#### 3.1. Catalyst characterization

XRD plots of  $\text{TiO}_2$ , MMT and Au-loaded  $\text{TiO}_2$  nano-composites are shown in Fig. 3(a). The peaks of  $\text{TiO}_2$  calcined at 500 °C revealed a pure anatase and crystalline phase. The XRD plot of MMT presents a broad basal reflection of (0 0 1) at  $2\theta = 3.70^\circ$ , originated due to stacking disorder of MMT loaded

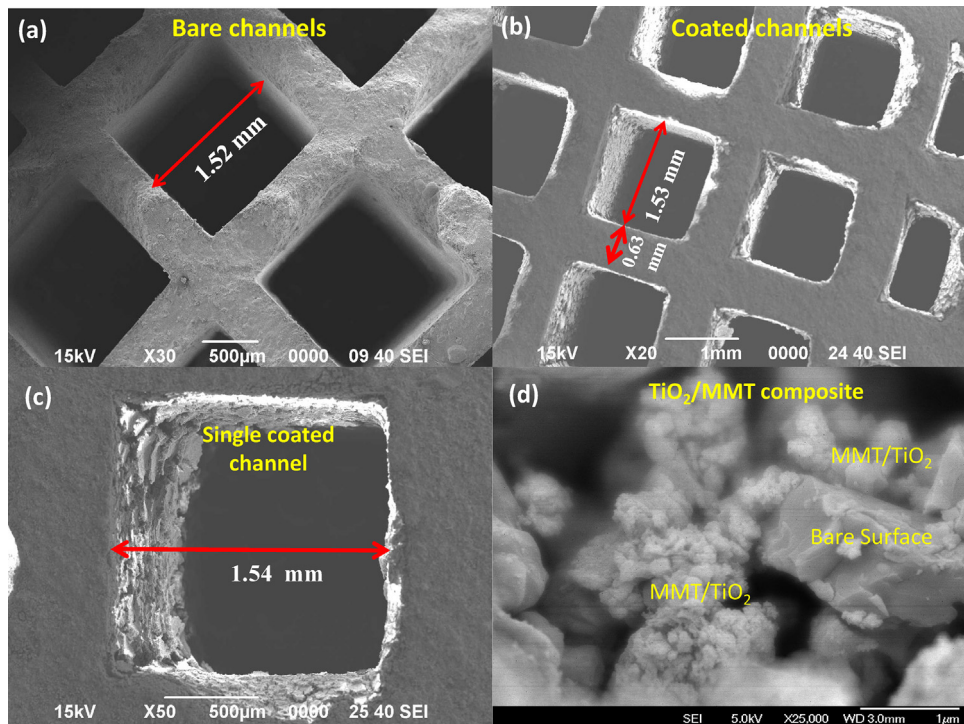


**Fig. 4.** SEM images of bare monolith and catalyst coated monolith channels: (a) bare monolith channels; (b) catalyst coated monolith channels, (c) catalyst coated over single channel, (d) catalyst morphology over the channel surface.

TiO<sub>2</sub> samples, TiO<sub>2</sub> persisted its original reflection with no additional peak appeared, however, all TiO<sub>2</sub> peaks become broader and weaker. This was probably, MMT hindered TiO<sub>2</sub> crystal growth, resulting in reduced crystallite size [21]. The prominent MMT peak (001) due to the layered clay has disappeared in all the MMT loaded TiO<sub>2</sub> samples. This revealed MMT layered structure disordered in the composite structure and similar observations were reported previously [21]. In the case of Au-loaded MMT/TiO<sub>2</sub> samples, delaminated MMT/TiO<sub>2</sub> structure with anatase phase of TiO<sub>2</sub> has been obtained. The peaks relating to Au, in the MMT/TiO<sub>2</sub> samples, in metal or oxide state were not detected, as the amount of Au-loaded was below the equipment detection limit. Additional information regarding phase change of the nanomaterials were obtained using Raman spectroscopy.

The phase identification of the TiO<sub>2</sub>, MMT/TiO<sub>2</sub> and Au-doped MMT/TiO<sub>2</sub> samples was further examined using Raman spectroscopy performed in the range of 100–1000 cm<sup>-1</sup> and the results are presented in Fig. 3(b). Pure TiO<sub>2</sub> reveals intense Raman signal with E<sub>g(1)</sub> mode appeared at 142 cm<sup>-1</sup> followed by less intense signals with modes E<sub>g(2)</sub> and E<sub>g(3)</sub> observed at 196 cm<sup>-1</sup> and 634 cm<sup>-1</sup>, respectively. Similarly, B<sub>1g</sub> peak appeared at 394 cm<sup>-1</sup> and mode (A<sub>1g</sub> + B<sub>1g</sub>) detected as a single merged peak at 513 cm<sup>-1</sup>. All these observations reflect the presence of pure anatase phase TiO<sub>2</sub> [48]. The Raman spectra of MMT/TiO<sub>2</sub> and Au-loaded MMT/TiO<sub>2</sub> samples are identical to the pure TiO<sub>2</sub>, which clearly indicated that TiO<sub>2</sub> retained its original structure after loading with Au and MMT. Furthermore, signals relating to MMT or Au in the MMT/TiO<sub>2</sub> or Au-MMT/TiO<sub>2</sub> composite samples were not identified. This was because of the uniform dispersion of MMT in the TiO<sub>2</sub> or their weak Raman scattering and probably due to relatively low concentration of Au. However, changes were obvious in the position with broadened peaks. With MMT and Au loading, the Raman bands E<sub>g(1)</sub> were shifted towards higher wavenumber in all the modified TiO<sub>2</sub> samples (e.g., 149 cm<sup>-1</sup> for MMT/TiO<sub>2</sub>) and similar observation have been reported previously [49]. The findings of Raman analysis has

established successful loading of Au over the MMT-dispersed TiO<sub>2</sub> structure without any phase change.

The morphology of cordierite support was investigated by SEM as demonstrated in Fig. 4. The bare monolith channels of cordierite structure with channel diameter 1.52 mm are obvious in Fig. 4(a). Fig. 4(b) reveals uniformly coated catalyst over the channels surface with no broken layers. The structure of single channel with catalyst coated over the surface is obvious in Fig. 4(c). Therefore, a good dispersion of catalysts over the monolith surface with thickness of 10–20 μm can be achieved using sol-gel dip-coating method. Fig. 4(d) depicts the structure of MMT/TiO<sub>2</sub> composite coated over the channel surface.

The morphology of MMT, TiO<sub>2</sub>, MMT/TiO<sub>2</sub> and Au-modified MMT/TiO<sub>2</sub> nanoparticles was investigated by FESEM and results are exhibited in Fig. 5. The MMT image in Fig. 5(a–b) shows stacked MMT layers with disorder structures. Fig. 5(c) reveals spherical shape and uniform size of TiO<sub>2</sub> nanoparticles. Fig. 5(d) illustrates images of TiO<sub>2</sub> dispersion over the MMT layers. Evidently, MMT layers were completely destroyed and TiO<sub>2</sub> NPs are well distributed over the MMT surface, thus producing MMT/TiO<sub>2</sub> nanocomposite structure. The morphology of Au-loaded MMT/TiO<sub>2</sub> sample is much similar to MMT/TiO<sub>2</sub> composite, where MMT layers are destroyed as presented in Fig. 5(e–f). The EDX mapping of Au nanoparticles deposited on the surface of MMT/TiO<sub>2</sub> composite catalyst is given in Fig. 5(g–h). From the elemental mapping mode, highly and uniformly dispersed Au nanoparticles over the MMT/TiO<sub>2</sub> structure were observed. This implied good interaction between Au and TiO<sub>2</sub> for efficient charges separation. The composition of elements revealed the presence of Au, Mn and Fe metals in addition of Si, Al, Ti and O elements due to MMT/TiO<sub>2</sub> composite. Due to the presence of these metal elements, there can be proficient charges separation promoted by MMT metal ions (Mn, Fe) and Au in the TiO<sub>2</sub> structure.

The transmission electron microscopy (TEM) images of MMT-dispersed Au/TiO<sub>2</sub> are shown in Fig. 6. The mesoporous structure of TiO<sub>2</sub> nanoparticles dispersed in MMT is depicted in Fig. 6(a–b). Fig. 6(c–d) displayed uniform dispersion of TiO<sub>2</sub> nanoparticles

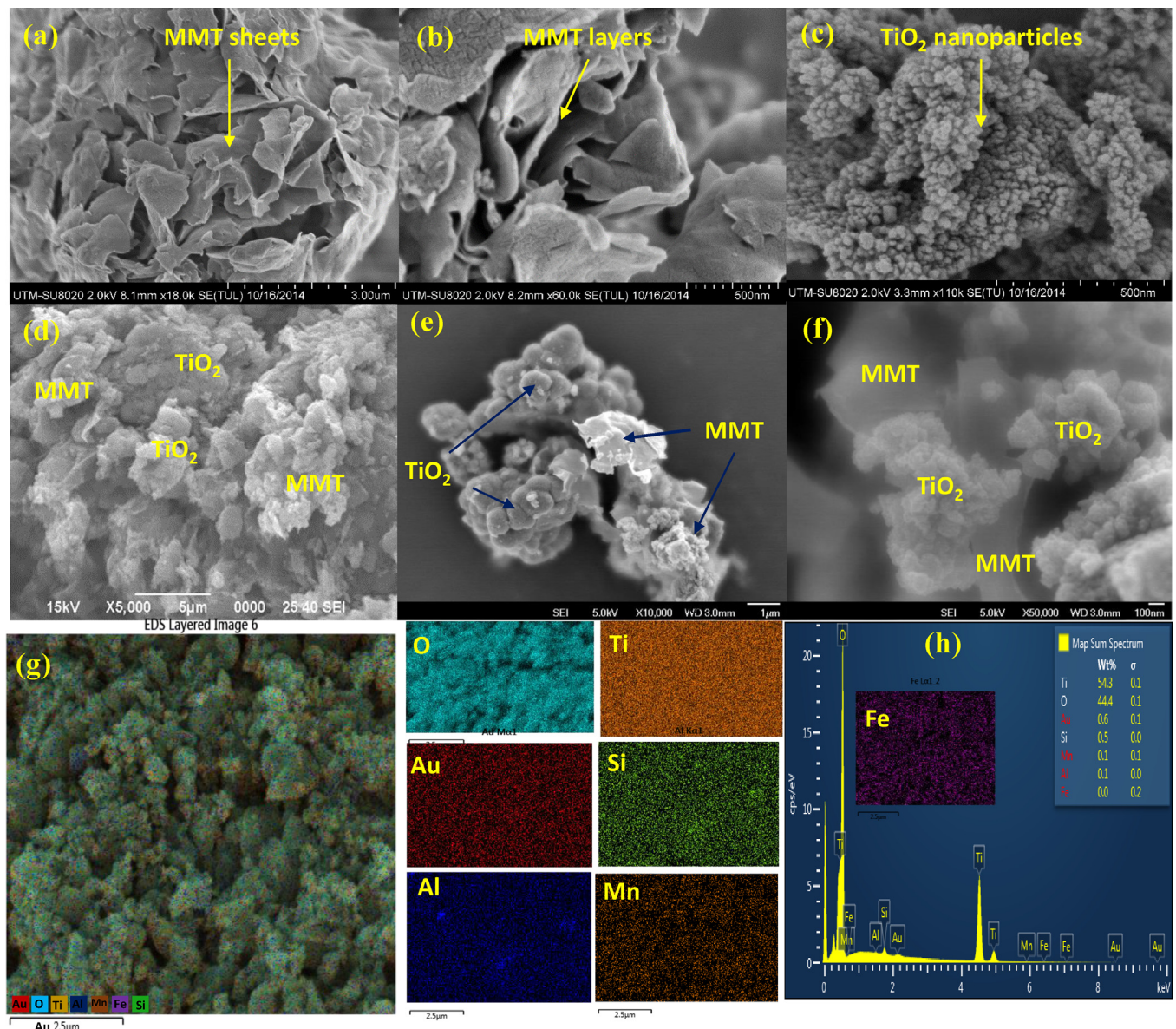


**Fig. 5.** FESEM images of MMT, TiO<sub>2</sub> and Au/MMT modified TiO<sub>2</sub> samples: (a–b) SEM images of MMT layers; (c) SEM image of TiO<sub>2</sub> nanoparticles, (d) SEM image of TiO<sub>2</sub>/MMT sample, (e–f) SEM of Au-MMT/TiO<sub>2</sub> samples, (g) EDX mapping distribution of elements, (h) EDX plot for elements composition.

inside MMT structure. The existence of TiO<sub>2</sub> in MMT structure is obvious. The lattice fringe spacing of 0.35 nm was observed, corresponds to plan (101) of anatase TiO<sub>2</sub>, as depicted in Fig. 6(e). The fringe spacing for Au was not identified, evidently due to lower Au contents and uniform dispersion in the MMT/TiO<sub>2</sub> composite sample and similar observations have been reported previously [50]. The Selected Area Electron Diffraction (SEAD) pattern of TiO<sub>2</sub> is depicted in Fig. 6(f). The first four rings are assigned to (101), (004), (200), (105) reflections of pure anatase phase of TiO<sub>2</sub> in the composite sample. The SAED patterns are in good agreement with XRD and Raman measurements.

X-ray photo-electron spectroscopy (XPS) of 0.5% Au-10% MMT/TiO<sub>2</sub> catalyst is depicted in Fig. 7. The survey spectra is presented in Fig. 7(a). The Ti 2p spectra peaks with binding energies 457.94 eV and 463.65 eV assigned to Ti 2p<sub>3/2</sub> and Ti 2p<sub>1/2</sub>, respectively, both of which correspond to Ti<sup>4+</sup> oxidation states or TiO<sub>2</sub>. Fig. 7(c) shows less intense peaks of Au and best fitting observed with binding energies 83.99 eV and 87.13 eV corresponds to Au 4f<sub>5/2</sub> and Au 4f<sub>3/2</sub>, suggesting Au exists in the metal state [51]. The further

confirmation about the existence of Au in metal state was identified by UV-vis analysis. Broad oxygen spectra in Fig. 7(d) showed O 1s peak located around 531.49 eV which reflects the presence of OH group over the surface of TiO<sub>2</sub>. Fig. 7(e) shows carbon peaks with binding energy 284.6 eV assigned to elemental carbon (C=C), while peak at 288 eV reflects the presence of C=O. The Si 2p peaks with binding energies located at 99.43 and 108.25 eV and Al 2p peaks located at 74.20 eV reflects interaction between Si/Al due to their presence in MMT as shown in Fig. 7(f and g). The presence of Mn and N corresponding to presence of transition metals and metal ions inside MMT galleries as depicts in Fig. 7(h and i) [21].

Fig. 8 shows UV-vis diffuse reflectance spectra (DRS) of TiO<sub>2</sub>, MMT/TiO<sub>2</sub> and Au-modified MMT/TiO<sub>2</sub> samples and digital photographs of the corresponding samples. The obtained TiO<sub>2</sub> has white in colour while MMT has tinted with yellow or green colour, however, Au-doped MMT/TiO<sub>2</sub> samples were purple in colour and differ in colour density as depicted in Fig. 8(a). The absorbance spectra of both TiO<sub>2</sub> and MMT/TiO<sub>2</sub> samples showed intense absorption below 400 nm. However, Au-loaded MMT/TiO<sub>2</sub> samples gave broad

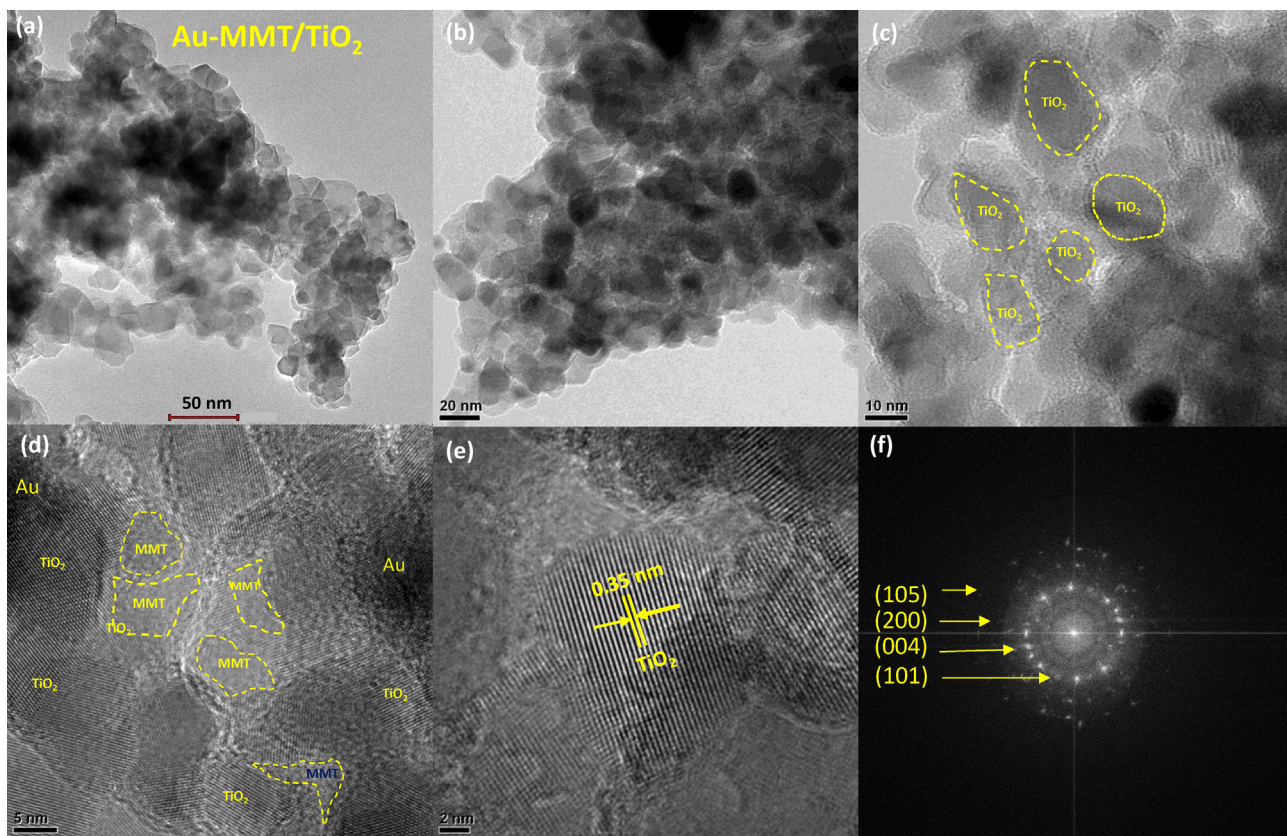


**Fig. 6.** TEM images of MMT-dispersed Au/TiO<sub>2</sub> nanoparticles: (a–b) Mesoporous MMT/TiO<sub>2</sub> structure, (c–d) TiO<sub>2</sub> dispersed over MMT, (e) d-spacings of TiO<sub>2</sub>, (f) SAED patterns of TiO<sub>2</sub>.

absorption features, which is assigned to Localized Surface Plasmon Resonance (LSPR) peak of metallic Au-NPs exist in the composite sample. Au-NPs in MMT/TiO<sub>2</sub> composite give standard reflection with peak located at ~580 nm due to LSPR of Au-NPs [36]. The band gap energy, according to plot of  $(\alpha h\nu)^2$  vs photon energy (eV). Both TiO<sub>2</sub> and MMT/TiO<sub>2</sub> samples have band gap of 3.11 eV and 3.09 eV, respectively, while band gap energy of ~3.05 eV obtained in Au-loaded MMT/TiO<sub>2</sub> samples. The negligible difference in band gap energies would be due to reduce in the TiO<sub>2</sub> crystal size [46]. This revealed MMT and Au loading did not alter substantially the absorption properties of TiO<sub>2</sub> samples and similar observations have been reported previously [29,52]. Therefore, photoactivity of composite sample under visible light irradiations would be due to LSPR effect of Au-NPs. More importantly, the illuminations due to LSPR of Au NPs could be seen when the samples were excited with a laser beam of wavelength 532 nm, as depicted in Fig. 8(c–d). The visible light irradiation has no effect on MMT/TiO<sub>2</sub> sample (Fig. 8c), yet, emitting of light due to LSPR of Au could be seen in Fig. 8(d). These observations have confirmed LSPR of Au NPs in MMT/TiO<sub>2</sub> composite sample and could be used under simulated solar energy.

Fig. 9(a) presents FTIR peaks of TiO<sub>2</sub>, MMT and Au-loaded MMT/TiO<sub>2</sub> samples. The spectra of TiO<sub>2</sub> with bands appeared at 1625 cm<sup>-1</sup> and 3428 cm<sup>-1</sup>, indicating chemisorbed H<sub>2</sub>O in TiO<sub>2</sub> and –OH stretching vibration. The MMT spectra showed various peaks at different locations. The stretching band at 3633 cm<sup>-1</sup> attributed to Al<sub>2</sub>OH group of octahedral layer in MMT, while peaks at 3428 cm<sup>-1</sup> and 1625 cm<sup>-1</sup> pertaining to stretching and bending vibration of hydroxyl group of water molecules on the external layer of MMT. Furthermore, C–H stretching vibration of the organic modifiers in MMT structure appeared at 2926 cm<sup>-1</sup> and 2839 cm<sup>-1</sup>. Asymmetric vibration of SiO<sub>2</sub> tetrahedral layer in MMT can be identified at 1049 cm<sup>-1</sup>, yet several peaks between 1000 and 500 cm<sup>-1</sup>

**Table 1**  
Summary of physicochemical analysis of TiO<sub>2</sub> and Au/MMT-modified TiO<sub>2</sub> samples.

Sample	BET surface area	BJH pore volume	Pore width
	(m <sup>2</sup> /g)	(cm <sup>3</sup> /g)	(nm)
TiO <sub>2</sub>	43	0.135	11
MMT	2	0.142	30
10% MMT/TiO <sub>2</sub>	52	0.103	9
0.2% Au-10% MMT/TiO <sub>2</sub>	54	0.251	8
0.5% Au-10% MMT/TiO <sub>2</sub>	51	0.266	7
1.0% Au-10% MMT/TiO <sub>2</sub>	46	0.123	8

attributed to Al-IV tetrahedra. The stretching vibration bands of MMT/TiO<sub>2</sub> and Au-MMT/TiO<sub>2</sub> have similar reflections with the pure TiO<sub>2</sub> with stretching band at 3633 cm<sup>-1</sup> due to Al<sub>2</sub>OH group and 1049 cm<sup>-1</sup> due to asymmetric stretching vibration of SiO<sub>2</sub> tetrahedra.

Fig. 9(b) depicts N<sub>2</sub> adsorption-desorption analysis of MMT, TiO<sub>2</sub> and Au-loaded MMT/TiO<sub>2</sub> samples. In pure MMT sample, no typical porous characteristics was observed in the N<sub>2</sub> adsorption-desorption isotherms. This was probably due to irregular structure of pores and galleries in the layered structured MMT material or the equipment was not compatible for MMT analysis. However, all the isotherms of Au and MMT modified TiO<sub>2</sub> samples show a type IV with high volume of N<sub>2</sub> adsorption at relatively high pressure (P/P<sub>0</sub>) region. Monolayer/multilayer adsorption is obvious at relatively low pressure (low P/P<sub>0</sub>). On the other hand, capillary condensation is obvious on the upper part of isotherms at relatively high pressure (high P/P<sub>0</sub>).

The summary of surface areas, pore volumes and pore sizes of TiO<sub>2</sub>, MMT, MMT/TiO<sub>2</sub> and Au-loaded MMT/TiO<sub>2</sub> samples are presented in Table 1. The specific surface area ( $S_{BET}$ ) of 43 m<sup>2</sup> g<sup>-1</sup> was obtained in the case of pure TiO<sub>2</sub>, increased to 52 m<sup>2</sup> g<sup>-1</sup>

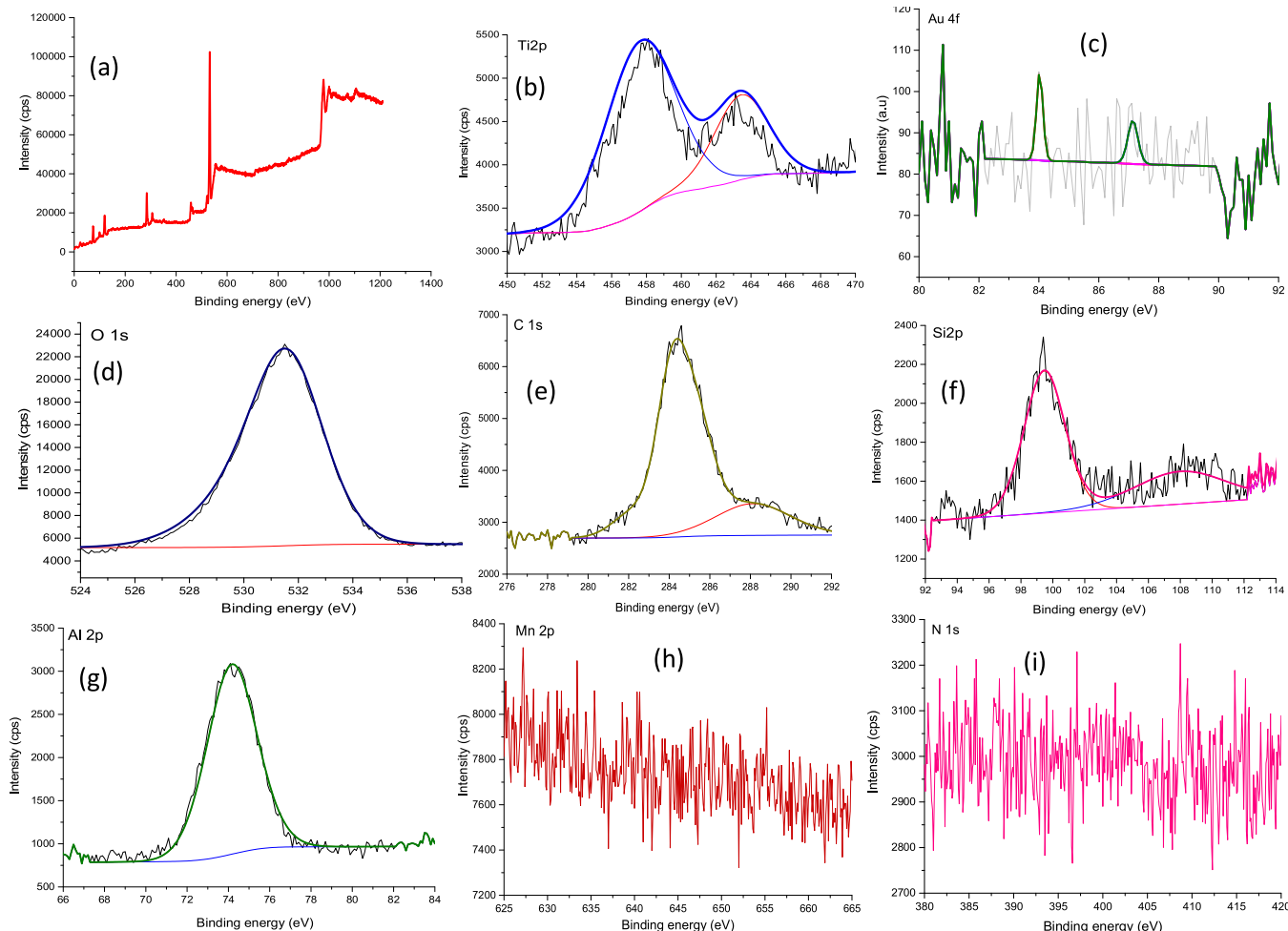


**Fig. 7.** XPS spectra of 0.5% Au-10% MMT/TiO<sub>2</sub> nanocomposite (a) Survey spectra, (b) spectra of Ti 2p, (c) Au 4f, (d) O 1s, (e) C 1s, (f) Si 2p, (g) Al 2p, (h) Mn 2p, and (i) N 1s.

for 10 wt.% MMT/TiO<sub>2</sub> sample. On the other hand, BET surface area was increased to 54 m<sup>2</sup>/g in 0.2% Au loading, but gradually decreased to 51 and 46 m<sup>2</sup>/g in 0.5% and 1.0% Au-loading MMT/TiO<sub>2</sub> samples. However, BJH pore volume increased in Au-loaded MMT/TiO<sub>2</sub> samples, confirming mesoporous structure of these materials. Besides, pore diameter of pure TiO<sub>2</sub> was 11 nm, decreased to 9 and 7 nm in MMT and Au-loaded MMT/TiO<sub>2</sub> samples, respectively. This revealed Au and MMT have an impact on the crystal growth of TiO<sub>2</sub>, resulting in improved morphology.

Fig. 9(c) shows PL emission spectra of the pure TiO<sub>2</sub>, MMT/TiO<sub>2</sub> and Au-modified MMT/TiO<sub>2</sub> samples excited at a wavelength of 325 nm. The PL signals can be attributed to the transition of electrons from the oxygen vacancies to TiO<sub>2</sub> valence band. It is noticeable that emission spectra of the Au and MMT-modified TiO<sub>2</sub> samples are similar to those of the pure TiO<sub>2</sub> sample. However, the PL intensity enfeebled in MMT and Au modified TiO<sub>2</sub> samples, resulting in hindered charges recombination rate by the presence of Au and MMT. More importantly, PL intensity in MMT/TiO<sub>2</sub> sample was lower, which revealed MMT has an impact on preventing charges recombination rate due to presence of metal ions (e.g., Mn, Fe) inside its galleries. Therefore, significantly enhanced photoactivity of Au-MMT/TiO<sub>2</sub> composite would probably be due to synergistic effect of Au and MMT inside TiO<sub>2</sub> structure.

### 3.2. Photocatalytic CO<sub>2</sub> reduction with H<sub>2</sub>

Before photocatalytic CO<sub>2</sub> reduction experiments, quality control analysis were conducted to confirm products were originated

during photo-reduction of CO<sub>2</sub> only. All the catalysts were tested in a gas phase system using high purity helium (He ~99.99%). Using only helium carrier gas (in the absent of CO<sub>2</sub> and H<sub>2</sub>), carbon containing compounds were not detected by the catalyst samples under light irradiations. Therefore, all the products in the experiment must be produced during CO<sub>2</sub> reduction through photocatalytic reaction.

In this work, three basic samples namely bare TiO<sub>2</sub>, MMT/TiO<sub>2</sub> and Au-MMT/TiO<sub>2</sub> deposited over the monolithic support were fabricated as depicted in Fig. 10(a). Using bare TiO<sub>2</sub>, there were more production of electrons due to higher light harvesting inside monolith channels. However, these photo-generated electrons could recombine immediately due to the absent of electrons sink. In MMT-dispersed TiO<sub>2</sub> sample, recombination of electrons can be somewhat hindered by metals ions present in MMT as evidenced by EDX, XPS and PL analysis. However, a good separation of electrons can be achieved over highly dispersed MMT/TiO<sub>2</sub> composite with Au-loading. In this case, a Schottky contact is developed between Au and TiO<sub>2</sub>, where the electron transfer depends on the size of Au-NPs: for example small Au-NPs improve the electron transfer, however, large size Au-NPs could activate TiO<sub>2</sub> under visible or UV-light irradiations via LSPR effect and metallic interband transitions, respectively [50,53,54].

Dynamic photocatalytic CO<sub>2</sub> reduction to CO over TiO<sub>2</sub>, MMT/TiO<sub>2</sub> and Au-loaded MMT/TiO<sub>2</sub> samples at different irradiation times is demonstrated in Fig. 10(b). Evidently, CO was detected as the main product over all types of photo-catalysts which confirmed favorable reaction for selective CO production over all the

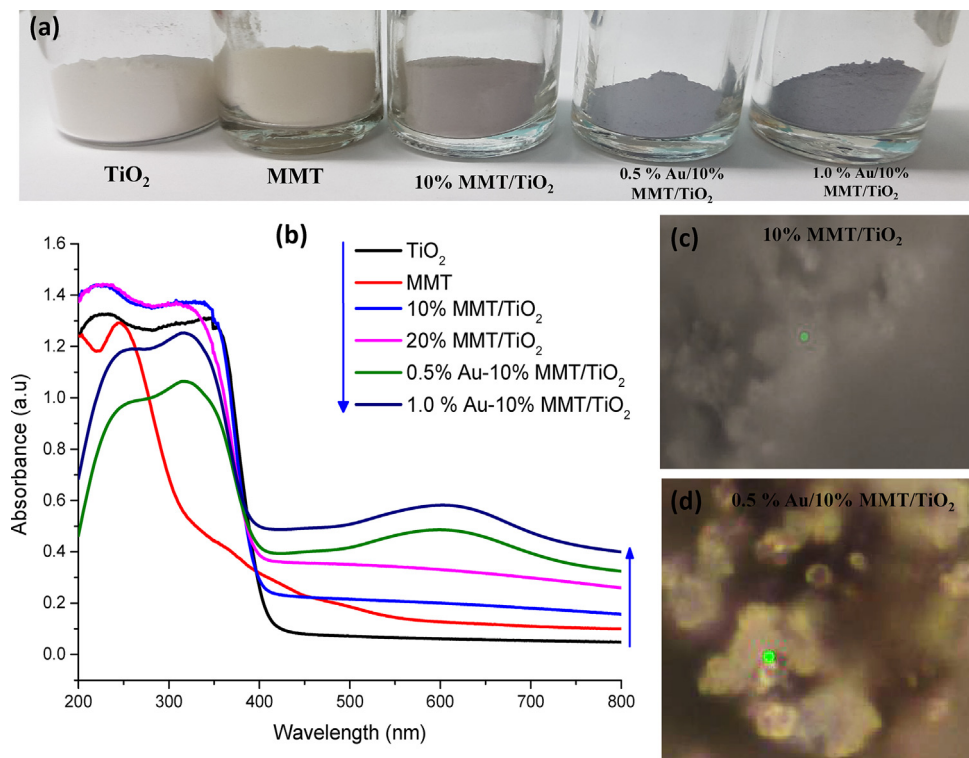


**Fig. 8.** (a) Digital images of powder photocatalyst samples; (b) UV-vis diffuse reflectance absorbance spectra of  $\text{TiO}_2$ , MMT and Au-MMT/ $\text{TiO}_2$  samples. (c-d) Photographs of the illuminations of powder photo-catalysts due to MMT/ $\text{TiO}_2$  and LSPR of Au-NPs excited with a laser beam of wavelength 532 nm.

samples while using monolith as a support and hydrogen as a reducing agent. Pure  $\text{TiO}_2$  has low photo-activity for CO production, which was increased in 10 wt.% MMT dispersed  $\text{TiO}_2$  sample. This was obviously due to hindered charges recombination rate and efficient  $\text{CO}_2$  adsorption in MMT structure. Interaction between MMT transition metal ions (e.g., Fe, Mn) and  $\text{TiO}_2$  dispersed over MMT surface and inside galleries enables hindrance of charges recombination rate [21]. However, efficiency was not much significant as the transfer rate of electrons from interior to the catalyst surface was not much appreciable.

Noticeably, much higher CO production was detected when Au was loaded into MMT/ $\text{TiO}_2$  sample. The optimal Au-loading of 0.5 wt.% was observed at which highest amount of CO was produced. This considerably improved photo-activity of Au-loaded MMT/ $\text{TiO}_2$  sample was due to synergistic effect between MMT metal ions and Au resulting in efficient charges separation with hindered recombination rate. The electrons trapped by MMT transition metal ions ( $M^+$ ) within the MMT structure dispersed within  $\text{TiO}_2$  can be transferred towards Au. Therefore, the enhanced CO production by the composite sample can be explained by the fact that Au-NPs decrease the electron hole recombination rate and transport electrons towards  $\text{CO}_2$  for its reduction and similar observations have been reported previously [55,56]. In addition,  $\text{TiO}_2$  could also be activated under UV-light irradiation due to metallic interband transition, resulting in more production of electrons over the  $\text{TiO}_2$  surface [34]. Due to this synergistic effect in Au-MMT/ $\text{TiO}_2$  catalyst loaded over monolithic support, it would be able to promote the efficiency of  $\text{CO}_2$ -hydrogen reaction system for dynamic and selective CO production. Furthermore, initially CO was energetically produced due to efficient  $\text{CO}_2$  adsorption over the fresh catalyst loaded over the monolithic support. However, over the time span, intermediate products would probably deposited over the catalyst surface, resulting in declined in CO production rate.

The performance of MMT and Au on the photo-activity of  $\text{TiO}_2$  for photocatalytic  $\text{CO}_2$  conversion with  $\text{H}_2$  to  $\text{CH}_4$  is presented in

**Fig. 10(c).** Using pure  $\text{TiO}_2$ , small amount of  $\text{CH}_4$  was produced which gradually increased in Au-loaded MMT/ $\text{TiO}_2$  samples. The highest amount of  $\text{CH}_4$  yielded in 0.5% Au-loaded MMT/ $\text{TiO}_2$  samples. On the other hand, small amount of hydrocarbons were also detected in Au-MMT/ $\text{TiO}_2$  catalyst. This was perhaps due to instant charge separation resulting in prolonged recombination time of the photo-generated charges. Initially, highest amounts of  $\text{CH}_4$  and hydrocarbons observed, then decreased rapidly over the irradiation time. The declined in yield was probably due to oxidation of  $\text{CH}_4$  with  $\text{O}_2$  in the presence of monolithic nanocatalysts. Yet,  $\text{O}_2$  was not detected in the product mixture due to the limitation of GC configuration and similar observations have been reported previously [28].

The effect of UV and Visible light irradiations on the efficiency of 0.5% Au-10% MMT/ $\text{TiO}_2$  catalyst for photocatalytic  $\text{CO}_2$  reduction to CO and hydrocarbons is demonstrated in **Fig. 11**. **Fig. 11(a)** shows yield of CO during photo-reduction of  $\text{CO}_2$  by  $\text{H}_2$  over the irradiation time at 100 °C, feed flow rate 20 mL/min and  $\text{CO}_2/\text{H}_2$  molar feed ratio 1.0. Using both types of light irradiations, CO was detected as the main product with adequate amounts of  $\text{CH}_4$  and  $\text{C}_2\text{H}_6$  in a continuous flow monolith photoreactor. Interestingly, the amount of CO produced under UV-light was significantly higher than using simulated solar energy under the same operating conditions. Conversely, the generation of  $\text{CH}_4$  was significant using visible-light-irradiations compared to UV-light as depicted in **Fig. 11(b)**. More importantly, continuous production of CO,  $\text{CH}_4$  and  $\text{C}_2\text{H}_6$  detected over the irradiation time using solar energy. This was probably lower CO production rate provides more catalyst stability and less accumulations of intermediate products under visible light irradiations.

Furthermore, production of these products over the composite catalyst can be explained based on their band alignments. Since the band gap energy of  $\text{TiO}_2$  (3.20 eV) is significantly higher than the energy of visible light (e.g., 2.40 eV) as depicted in **Fig. 11(c)**, thus the yield of products would not be much appreciable. How-

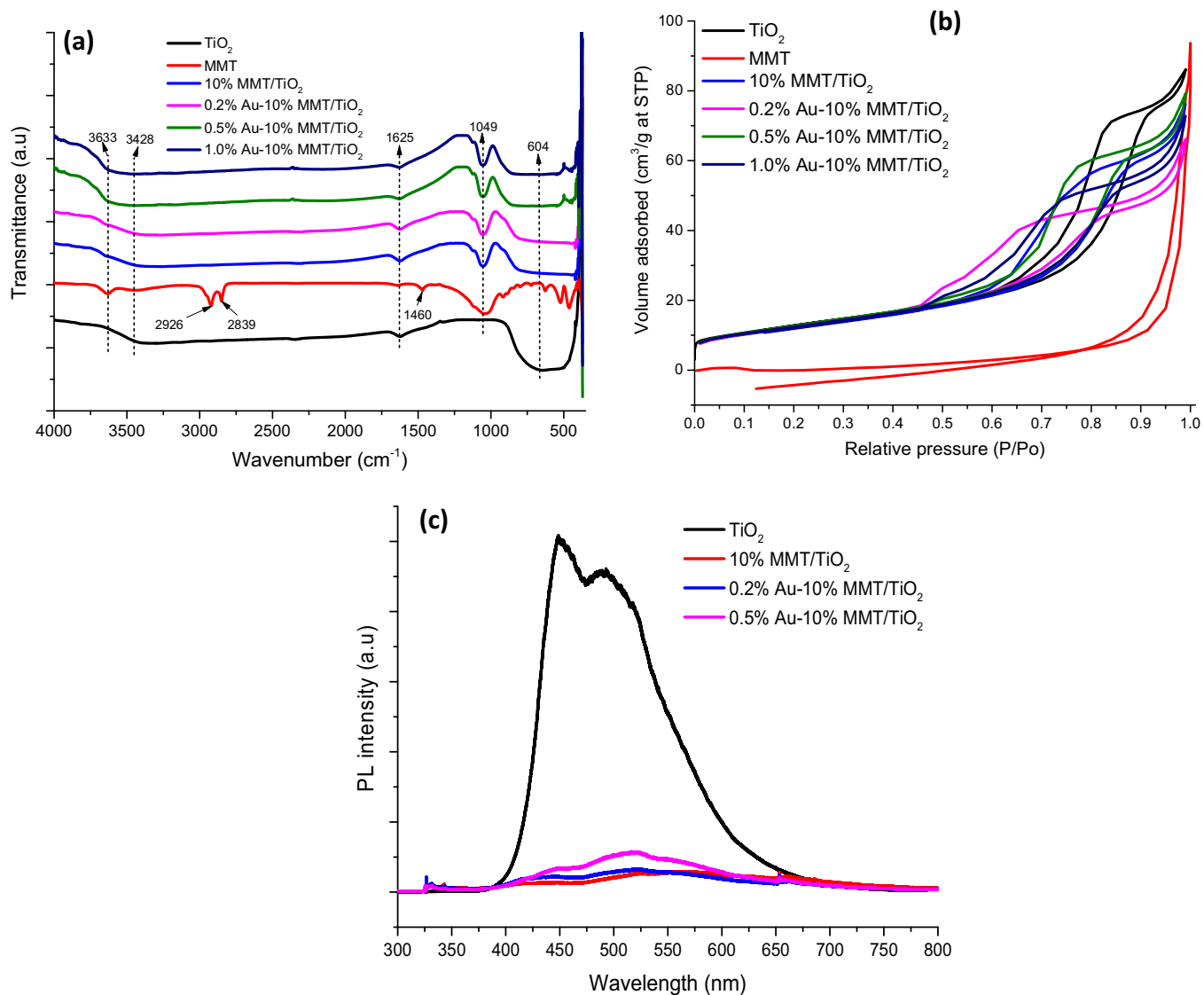


**Fig. 9.** (a) FTIR analysis of TiO<sub>2</sub>, MMT and Au-loaded MMT/TiO<sub>2</sub> samples; (b) N<sub>2</sub> adsorption–desorption isotherms of TiO<sub>2</sub>, MMT and Au-MMT/TiO<sub>2</sub> samples;(c) PL analysis of TiO<sub>2</sub>, MMT/TiO<sub>2</sub> and Au-doped MMT/TiO<sub>2</sub> samples.

**Table 2**

Summary of yield rates and selectivity of products over TiO<sub>2</sub> and modified TiO<sub>2</sub> samples.

Samples	Production rate <sup>a</sup> (μmole g-catal. <sup>-1</sup> h <sup>-1</sup> )					Selectivity <sup>b</sup> (%)	
	CO	CH <sub>4</sub>	C <sub>2</sub> H <sub>4</sub>	C <sub>2</sub> H <sub>6</sub>	C <sub>3</sub> H <sub>6</sub>	CO	CH <sub>4</sub>
TiO <sub>2</sub>	18	0.76	Nd	Nd	Nd	95.95	4.05
10% MMT/TiO <sub>2</sub>	51	1.10	Nd	0.07	Nd	97.76	2.11
0.5% Au–10% MMT/TiO <sub>2</sub> <sup>c</sup>	1223	12	0.32	1.10	0.26	98.89	0.97
0.5% Au–10% MMT/TiO <sub>2</sub> <sup>d</sup>	199	42	Nd	2.08	Nd	81.86	17.28

<sup>a</sup> Production rate calculated on 2 h irradiation basis at CO<sub>2</sub>/H<sub>2</sub> molar ratio 1.0, T = 100 °C, Feed flow 20 mL/min.

<sup>b</sup> Selectivity of product C<sub>i</sub>(%) =  $\frac{\text{moles of } C_i \text{ in product mixture}}{\text{Total moles of } C \text{ produced}} \times 100$ . C<sub>i</sub> is the mole of carbon specie i (CO, CH<sub>4</sub>, C<sub>2</sub>H<sub>4</sub>, C<sub>2</sub>H<sub>6</sub>, and C<sub>3</sub>H<sub>6</sub>) in the products mixture and C is the mole of total carbon compounds produced.

<sup>c</sup> Yield rate of products under UV-light irradiations.

<sup>d</sup> Yield rate of products under simulated solar energy.

ever, significant amounts of CO, CH<sub>4</sub> and C<sub>2</sub>H<sub>6</sub> were produced due to intense local field produced due to plasmonic Au nanoparticles in MMT/TiO<sub>2</sub> catalyst. Consequently, under visible light irradiations, electron-hole pairs would be generated due to light absorption by Au nanoparticles. Since the conductance band of TiO<sub>2</sub> (CB = -0.50 eV) lies above the CO<sub>2</sub>/CH<sub>4</sub> reduction potential (-0.24 eV), it is energetically favourable for the transfer of electrons from the TiO<sub>2</sub> CB band to CO<sub>2</sub> for the production of CH<sub>4</sub>.

Previously, Hou et al. [34] reported CH<sub>4</sub> as the only favourable product during CO<sub>2</sub> reduction with H<sub>2</sub>O under visible light irradiation of wavelength 532 nm. Likewise, when the UV-light of wavelength 252 nm was employed, production of CO was further increased and the results can be described by comparing CB energy of TiO<sub>2</sub> with d-band energy of Au as depicted in Fig. 11(d). In noble metals, d-band electrons from the metals (e.g., Au) are transferred towards semiconductor surface (e.g., TiO<sub>2</sub>) via metallic interband transitions

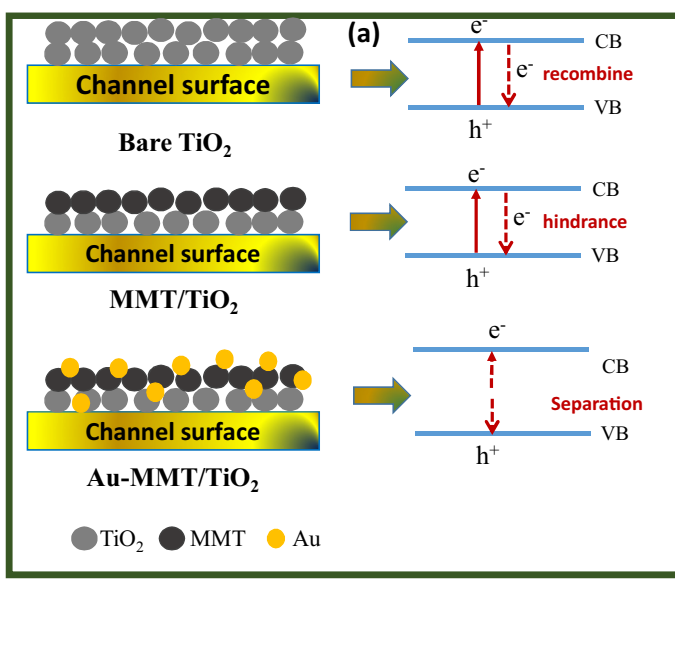
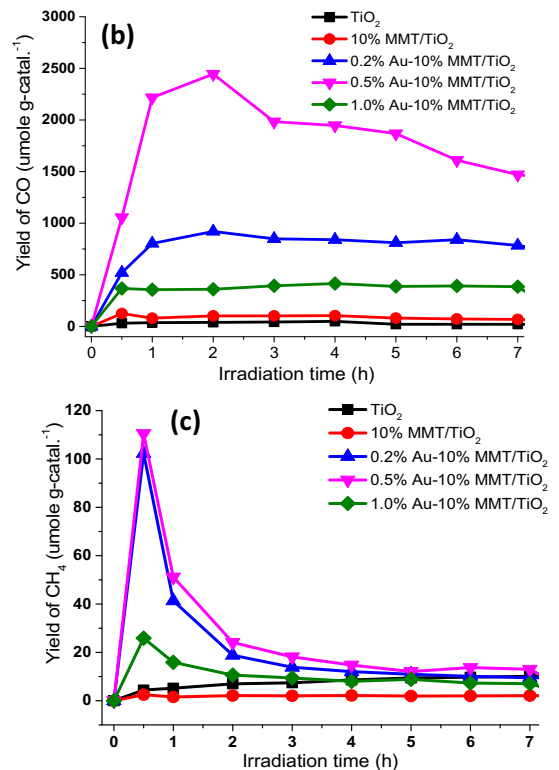


**Fig. 10.** (a) Schematic of three types of photo-catalysts supported over monolithic substrate; (b) Dynamic CO evolution; (c) CH<sub>4</sub> evolution over Au-TiO<sub>2</sub>/MMT samples at 100 °C, CO<sub>2</sub>/H<sub>2</sub> ratio 1.0 and feed flow 20 mL/min.

during the optical absorption process [57]. The light energy with wavelength irradiation of 252 nm (e.g., 4.88 eV) used in this study is more than the minimum energy required for the activation of Au to transfer electrons via interband transition [34]. Therefore, it is favourable to excite electrons from d-band of Au, which is above the CB of TiO<sub>2</sub> for the production of CO and hydrocarbons.

The yield rate and selectivity of different products are presented in Table 2. Using UV-light, the yield of CO over 0.5 wt.% Au–10 wt.% MMT/TiO<sub>2</sub> was 1223 μmole g-catal.<sup>-1</sup> h<sup>-1</sup>, a 24 times than the 10 wt.% MMT/TiO<sub>2</sub> and 68 fold than using pure TiO<sub>2</sub>. The enhanced photo-activity was noticeably due to fast charges transfer rate by Au with larger active surface sites over monolith channels [12]. The other products with appreciable amounts detected over Au-loaded MMT/TiO<sub>2</sub> were CH<sub>4</sub> and C<sub>2</sub>H<sub>6</sub> hydrocarbons. The selectivity for CO production over the TiO<sub>2</sub> increased from ~95.95 to 98.89% in Au-loaded MMT/TiO<sub>2</sub> sample. On the other hand, the amount of CO produced over 0.5% Au–10% MMT/TiO<sub>2</sub> catalysts under visible light was 199 μmole g-catal.<sup>-1</sup> h<sup>-1</sup>, a 6 folds lower than the amount of CO produced using UV-light irradiations under the same operating conditions. The production of CH<sub>4</sub> of 42 μmole g-catal.<sup>-1</sup> h<sup>-1</sup> were produced under visible light irradiations, ~3.5 folds the amount of CH<sub>4</sub> produced under UV-light irradiations. The selectivity of CO of 98.89% under UV-light was reduced to 81.86%, probably due to parallel reactions for the production of CH<sub>4</sub>. This was probably due to higher light intensity and strong penetration power of UV-light, some amount of CH<sub>4</sub> was also converted to CO in a dynamic monolith photoreactor. Therefore, lower amount of CH<sub>4</sub> was detected under UV-light than visible light irradiations. Based on these results, it is evident that CO<sub>2</sub> can efficiently be converted to fuels using Au-loaded MMT/TiO<sub>2</sub> catalyst and monolith photoreactor due to their synergistic effects under UV and Visible light irradiations.

The reusability of MMT-dispersed Au/TiO<sub>2</sub> catalyst was further investigated to evaluate the life of catalyst in a monolith photo-



reactor operating in a continuous mode. For reusability analysis of catalysts, experiments were conducted in cyclic runs under the identical conditions. Before starting the second cyclic run of the used catalyst, monolith was removed and put to open atmosphere for 1 h before starting the experiment. However, before starting third and fourth cyclic runs, the reactor was flushed with pure helium gas without removing the monolith as depicted in 12 (a). The stability analysis for photocatalytic CO<sub>2</sub> reduction to CO over 0.5 wt.% Au-loaded MMT/TiO<sub>2</sub> catalyst is depicted in Fig. 12(b). In the first and second run, CO production was similar and continuous over the entire irradiation times. More importantly, an increment in production could be observed in third and fourth cyclic run over the entire irradiation. This was possibly, after second run, catalyst was not exposed to oxygen, and thus Au was presented in reduced state. Therefore, enhanced photoactivity was due to reducibility of Au as explained in Eq. (1).



Eq. (1) presents reduction of AuO with H<sub>2</sub> to produce Au during photo-reduction process. The reduced Au have more ability for efficient separations of charges, resulting in improved activity for CO<sub>2</sub> reduction over the Au-MMT/TiO<sub>2</sub> catalyst loaded over monolithic support. The production of CH<sub>4</sub> and C<sub>2</sub>H<sub>6</sub> are depicted in Fig. 12(c-d). It is noticeable to see a continuous production of hydrocarbons over the entire irradiation due to prolonged photo-activity and stability of catalyst. Recently, we have reported photocatalytic CO<sub>2</sub> reduction to CO over copper and silver loaded TiO<sub>2</sub> photo-catalysts [33,58]. It was observed that catalyst lost photo-activity over the irradiation time and in cyclic runs. This was due to production of carbon specie (coke), which resulted in enhanced CH<sub>4</sub> and HCs production in cyclic runs. In the current study, stability of catalyst persisted till 44 h of irradiation time with no coke formation due to the presence of MMT and monolithic support. Therefore, enhanced photo-activity and stability of TiO<sub>2</sub>

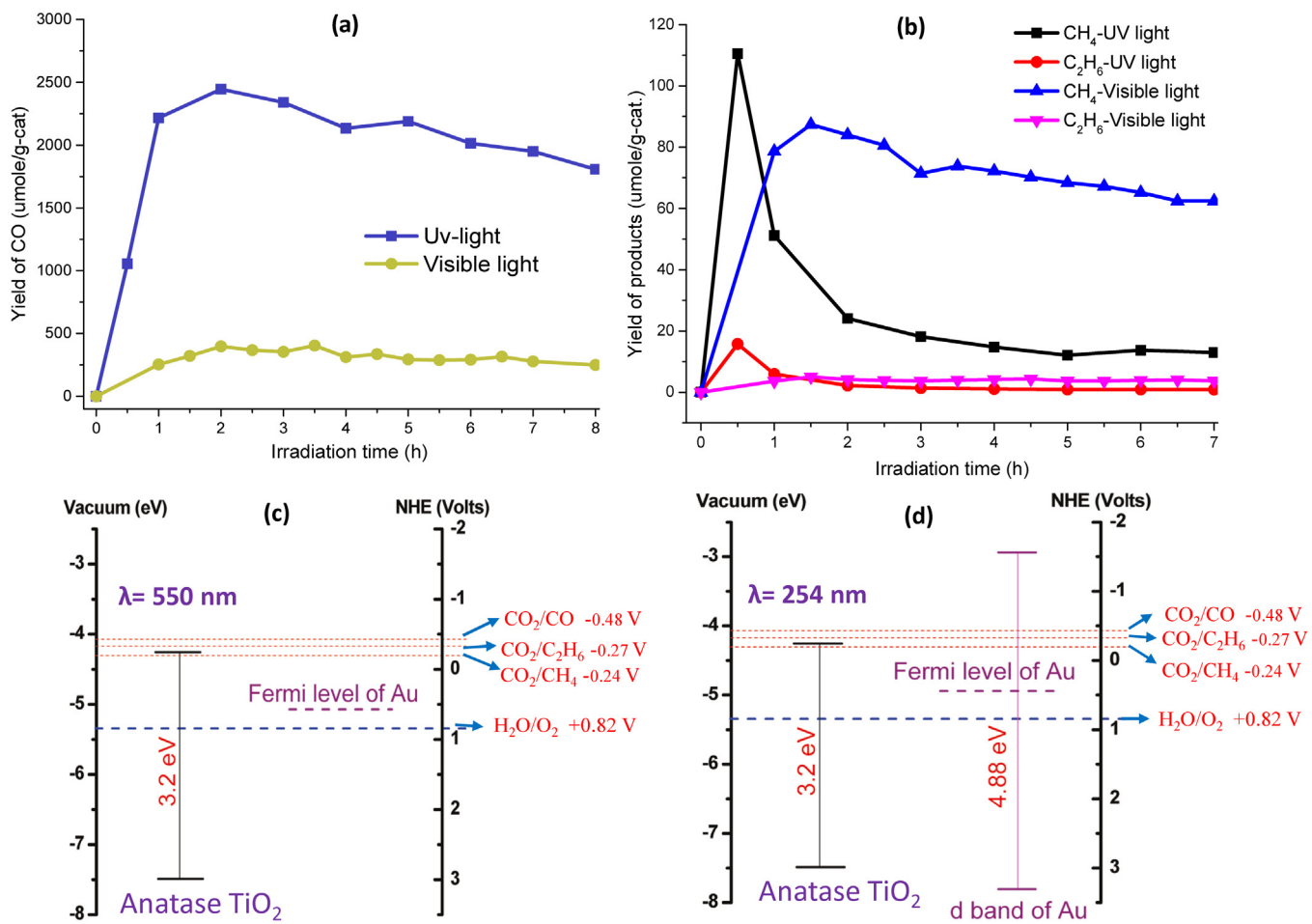
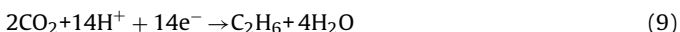
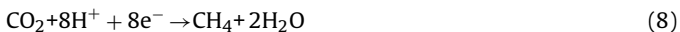


Fig. 11. Performance analysis of products yield of (a) CO and (b) hydrocarbons on 0.5% Au-10% MMT/TiO<sub>2</sub> catalyst under visible and UV-light irradiation; Energy band alignment of anatase TiO<sub>2</sub>, Au, and the relevant redox potentials of CO<sub>2</sub> under (c) solar energy; and (d) UV-light illumination.

modified with MMT/Au and loaded over monolithic support was evidently due to their synergistic effect, metal interband transition and higher photonic efficiency over monolithic support.

### 3.3. Reaction mechanism for CO<sub>2</sub> reduction

During photocatalytic CO<sub>2</sub> reduction reaction, CO<sub>2</sub> is reacted with H<sub>2</sub> for the CO production with smaller amounts of CH<sub>4</sub> and C<sub>2</sub>H<sub>6</sub> as the potential products over the Au-loaded MMT/TiO<sub>2</sub> catalyst as illustrated in Eqs. (2)–(9) [19].



First, when light was irradiated to photo-catalyst, electron-hole pairs were produced (Eq. 2). The photo-generated electrons were separated efficiently due to synergistic effect between MMT metal ions and Au, resulting in efficient separation of electrons as

explained in Eqs. (3) and (4). Next, electrons transferred toward CO<sub>2</sub> for its reduction while holes are consumed for H<sub>2</sub> oxidation as explained in Eqs. (5) and (6). The, H<sup>+</sup> radicals and active electrons can reduce CO<sub>2</sub> to CO, CH<sub>4</sub> and C<sub>2</sub>H<sub>6</sub> as explained in Eqs. (7)–(9).

These observations can be explained based on conductance band energy of TiO<sub>2</sub> with the reduction potential of CO<sub>2</sub> for the production of CO, CH<sub>4</sub> and C<sub>2</sub>H<sub>6</sub>. As discussed previously, CO was the main product with selectivity ~99%, confirming favourable CO<sub>2</sub> reduction process for CO production over Au-loaded MMT/TiO<sub>2</sub> catalyst loaded over monolithic support. As the CB of TiO<sub>2</sub> lies above the CO<sub>2</sub>/CO reduction potential, thus it energetically favourable for electrons from CB of TiO<sub>2</sub> to move to CO<sub>2</sub> for its reduction. The production of C<sub>2</sub>H<sub>6</sub> and CH<sub>4</sub> was not much significant since their reduction potentials are lower than the CB of TiO<sub>2</sub>. The amounts of CO produced over Au-MMT/TiO<sub>2</sub> was 68 fold more than the amount produced over the pure TiO<sub>2</sub>.

The schematic presentation of photo-catalytic CO<sub>2</sub> reduction to CO under UV and visible light irradiations is depicted in Fig. 13. Under visible light irradiation, TiO<sub>2</sub> was activated due to LSPR effect of Au nanoparticles. So the electrons can move easily towards the E<sub>CB</sub> of TiO<sub>2</sub> via Au-NPs during the optical absorption process. Thus, Au promotes light absorption and produces more electron/hole pairs in TiO<sub>2</sub> through the local electric field enhancement [35,53,59]. On the other hand, under UV-light ( $\lambda = 252$  nm), TiO<sub>2</sub> is activated due to d-bands of Au via metallic interband transitions which is favourable to excite electrons from d-band of Au toward E<sub>CB</sub> of TiO<sub>2</sub>. Over all, the enhanced photocatalytic activity of TiO<sub>2</sub> is

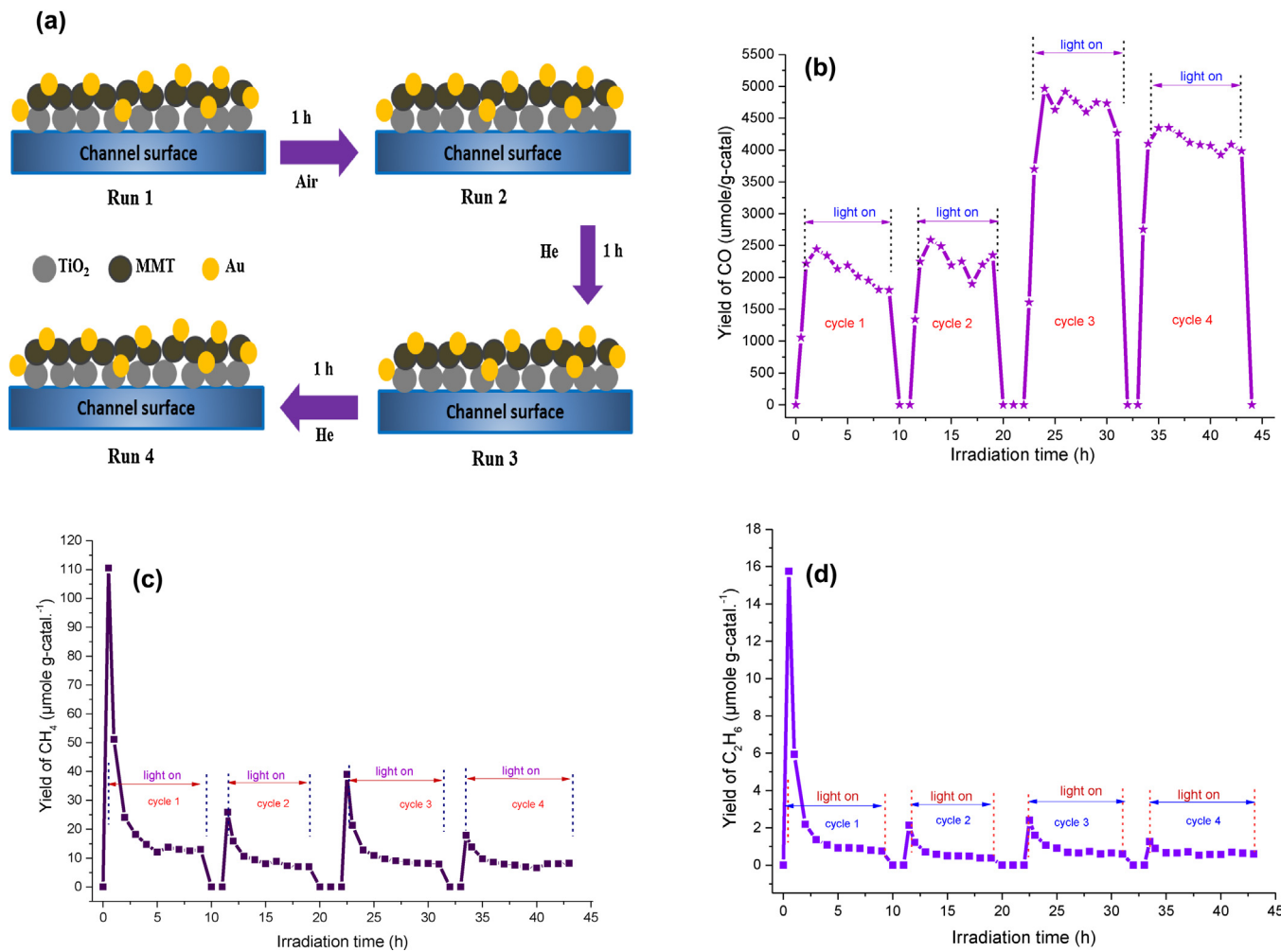


**Fig. 12.** (a) Schematic for the reactor flushed with pure helium gas without removing the monolith; (b) reusability analysis for CO production, (c) reusability analysis for CH<sub>4</sub> production; (d) reusability analysis for C<sub>2</sub>H<sub>6</sub> production in cyclic runs over 0.5% Au-10% MMT/TiO<sub>2</sub> catalyst at 100 °C, CO<sub>2</sub>/H<sub>2</sub> molar feed ratio 1.0 and feed flow rate 20 mL/min.

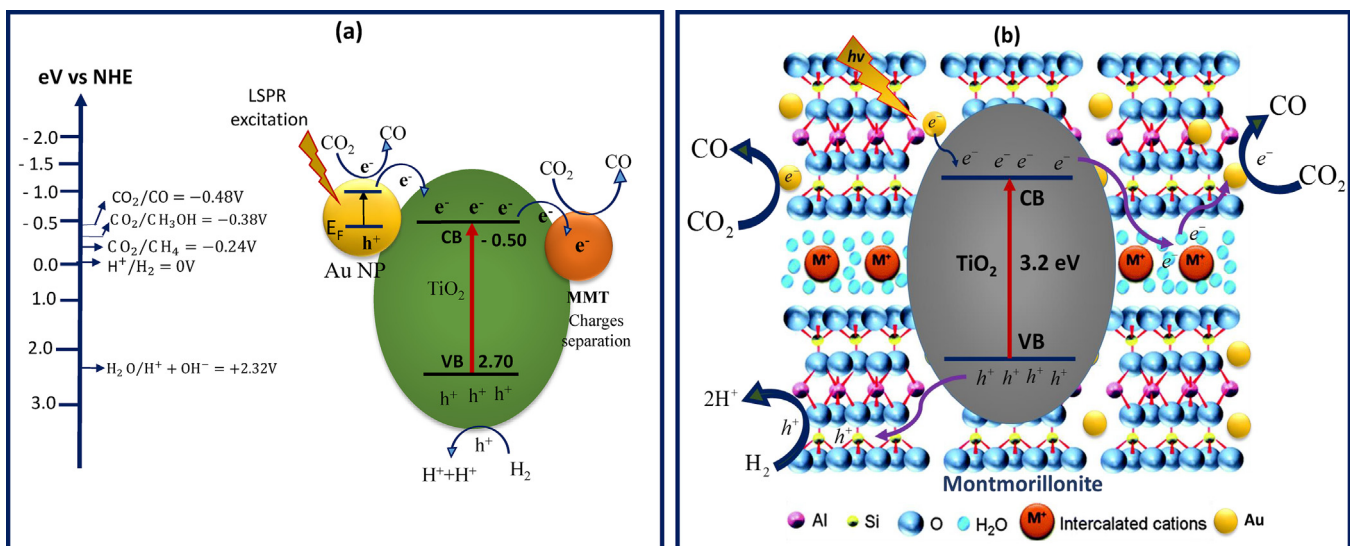


**Fig. 13.** (a) Energy band alignment of anatase TiO<sub>2</sub> for Plasmon enhanced CO<sub>2</sub> reduction under visible light illumination; (b) Schematic of reaction mechanism for photocatalytic CO<sub>2</sub> reduction with H<sub>2</sub> over MMT-dispersed Au/TiO<sub>2</sub> catalyst.

considered to be due to SPR effect of Au or due to d-band excitation as well as enhanced charges separation by loaded Au NPs. Furthermore, the electrons produced in the activated Au due to LSPR effect or captured by Au due to different particle sizes, can be utilized in CO<sub>2</sub> reduction reactions [38,54,56,60]. Therefore, in converting CO<sub>2</sub> to CO with Au-loaded MMT/TiO<sub>2</sub> system, the LSPR or d-band effect under visible and UV-light irradiating afforded by Au transport electrons to TiO<sub>2</sub>/MMT composite and enables to derive CO during CO<sub>2</sub> reduction process, resulting in enhanced photocatalytic activity.

#### 4. Conclusions

Photo-induced CO<sub>2</sub> reduction by H<sub>2</sub> for dynamic CO evolution over TiO<sub>2</sub> nanoparticles dispersed in MMT and loaded with Au was investigated. The yield rate of CO during CO<sub>2</sub> reduction was increased significantly by introducing Au and MMT into TiO<sub>2</sub>. The amount of CO as the key product observed over the Au-MMT/TiO<sub>2</sub> nanocomposite was 24 fold higher than MMT/TiO<sub>2</sub> and 68 fold the amount produced over the pure TiO<sub>2</sub> catalyst. This enhanced in photocatalytic activity under UV-light was due to metallic interband transition, efficient charges separation due to synergistic effect between MMT and Au, and larger illuminated surface area in a monolith photo-reactor. Plasmon-enhanced photo-catalytic CO<sub>2</sub> reduction under simulated solar energy was due to strong electric field created by LSPR of Au nanoparticles. The stability test revealed prolonged activity of the photo-catalyst supported over the monolith micro-channels, sustained even after 44 h of operation time. Therefore, cordierite monolithic support and Au/MMT could improve TiO<sub>2</sub> photo-activity, selectivity and stability for dynamic CO evolution during CO<sub>2</sub> reduction process.

#### Acknowledgement

This work was supported by Ministry of Higher Education (MOHE) Malaysia for the financial support of this research under FRGS (Fundamental Research Grant Scheme, Vote 4F876) and UTM RUG (University Technology Malaysia under Research University Grant, Vote 17H06).

#### References

- [1] S. Kiatphuengporn, W. Donphai, P. Jantaratana, N. Yigit, K. Föttinger, G. Rupprechter, M. Chareonpanich, Cleaner production of methanol from carbon dioxide over copper and iron supported MCM-41 catalysts using innovative integrated magnetic field-packed bed reactor, *J. Clean. Prod.* 142 (2017) 1222–1233.
- [2] M.-Q. Yang, Y.-J. Xu, Photocatalytic conversion of CO<sub>2</sub> over graphene-based composites: current status and future perspective, *Nanoscale Horiz.* 1 (2016) 185–200.
- [3] W. Yu, D. Xu, T. Peng, Enhanced photocatalytic activity of g-C<sub>3</sub>N<sub>4</sub> for selective CO<sub>2</sub> reduction to CH<sub>3</sub>OH via facile coupling of ZnO: a direct Z-scheme mechanism, *J. Mater. Chem. A* 3 (2015) 19936–19947.
- [4] Z.Q. He, J.T. Tang, J. Shen, J.M. Chen, S. Song, Enhancement of photocatalytic reduction of CO<sub>2</sub> to CH<sub>4</sub> over TiO<sub>2</sub> nanosheets by modifying with sulfuric acid, *Appl. Surf. Sci.* 364 (2016) 416–427.
- [5] M. Tahir, N.S. Amin, Performance analysis of nanostructured NiO–In<sub>2</sub>O<sub>3</sub>/TiO<sub>2</sub> catalyst for CO<sub>2</sub> photoreduction with H<sub>2</sub> in a monolith photoreactor, *Chem. Eng. J.* 285 (2016) 635–649.
- [6] Z. Xiong, Z. Lei, Z. Xu, X. Chen, B. Gong, Y. Zhao, H. Zhao, J. Zhang, C. Zheng, Flame spray pyrolysis synthesized ZnO/CeO<sub>2</sub> nanocomposites for enhanced CO<sub>2</sub> photocatalytic reduction under UV–Vis light irradiation, *J. CO<sub>2</sub> Util.* 18 (2017) 53–61.
- [7] A. Ahmad Beigi, S. Fatemi, Z. Salehi, Synthesis of nanocomposite CdS/TiO<sub>2</sub> and investigation of its photocatalytic activity for CO<sub>2</sub> reduction to CO and CH<sub>4</sub> under visible light irradiation, *J. CO<sub>2</sub> Util.* 7 (2014) 23–29.
- [8] J. Low, B. Cheng, J. Yu, Surface modification and enhanced photocatalytic CO<sub>2</sub> reduction performance of TiO<sub>2</sub>: a review, *Appl. Surf. Sci.* 392 (2017) 658–686.
- [9] P.-Q. Wang, Y. Bai, P.-Y. Luo, J.-Y. Liu, Graphene–WO<sub>3</sub> nanobelt composite: elevated conduction band toward photocatalytic reduction of CO<sub>2</sub> into hydrocarbon fuels, *Catal. Commun.* 38 (2013) 82–85.
- [10] Y. He, Y. Wang, L. Zhang, B. Teng, M. Fan, High-efficiency conversion of CO<sub>2</sub> to fuel over ZnO/g-C<sub>3</sub>N<sub>4</sub> photocatalyst, *Appl. Catal. B: Environ.* 168–169 (2015) 1–8.
- [11] P.N. Paulino, V.M.M. Salim, N.S. Resende, Zn–Cu promoted TiO<sub>2</sub> photocatalyst for CO<sub>2</sub> reduction with H<sub>2</sub>O under UV light, *Appl. Catal. B: Environ.* 185 (2016) 362–370.
- [12] M. Tahir, B. Tahir, Dynamic photocatalytic reduction of CO<sub>2</sub> to CO in a honeycomb monolith reactor loaded with Cu and N doped TiO<sub>2</sub> nanocatalysts, *Appl. Surf. Sci.* 377 (2016) 244–252.
- [13] Y. Kamemitsu, Y. Tamura, A. Nakajima, K. Okada, Preparation and properties of TiO<sub>2</sub>/montmorillonite composites, *Appl. Clay Sci.* 45 (2009) 20–23.
- [14] K.G. Bhattacharyya, S.S. Gupta, Influence of acid activation on adsorption of Ni(II) and Cu(II) on kaolinite and montmorillonite: kinetic and thermodynamic study, *Chem. Eng. J.* 136 (2008) 1–13.
- [15] Y. Li, J.R. Liu, S.Y. Jia, J.W. Guo, J. Zhuo, P. Na, TiO<sub>2</sub> pillared montmorillonite as a photoactive adsorbent of arsenic under UV irradiation, *Chem. Eng. J.* 191 (2012) 66–74.
- [16] J. Liu, M. Dong, S. Zuo, Y. Yu, Solvothermal preparation of TiO<sub>2</sub>/montmorillonite and photocatalytic activity, *Appl. Clay Sci.* 43 (2009) 156–159.
- [17] P. Praus, O. Kozák, K. Koci, A. Panacek, R. Dvorsky, CdS nanoparticles deposited on montmorillonite: preparation, characterization and application for photoreduction of carbon dioxide, *J. Colloid Interface Sci.* 360 (2011) 574–579.
- [18] K. Kočí, L. Matějová, O. Kozák, L. Čapek, V. Valeš, M. Reli, P. Praus, K. Šafářová, A. Kotarba, L. Obalová, ZnS/MMT nanocomposites: the effect of ZnS loading in MMT on the photocatalytic reduction of carbon dioxide, *Appl. Catal. B: Environ.* 158–159 (2014) 410–417.
- [19] M. Tahir, N.S. Amin, Photocatalytic reduction of carbon dioxide with water vapors over montmorillonite modified TiO<sub>2</sub> nanocomposites, *Appl. Catal. B: Environ.* 142–143 (2013) 512–522.
- [20] M. Tahir, N.S. Amin, Photocatalytic CO<sub>2</sub> reduction with H<sub>2</sub>O vapors using montmorillonite/TiO<sub>2</sub> supported microchannel monolith photoreactor, *Chem. Eng. J.* 230 (2013) 314–327.
- [21] M. Tahir, B. Tahir, N.S. Amin, Photocatalytic CO<sub>2</sub> reduction by CH<sub>4</sub> over montmorillonite modified TiO<sub>2</sub> nanocomposites in a continuous monolith photoreactor, *Mater. Res. Bull.* 63 (2015) 13–23.
- [22] M.M. Gui, W.M.P. Wong, S.P. Chai, A.R. Mohamed, One-pot synthesis of Ag–MWCNT@TiO<sub>2</sub> core-shell nanocomposites for photocatalytic reduction of CO<sub>2</sub> with water under visible light irradiation, *Chem. Eng. J.* 278 (2015) 272–278.
- [23] B.S. Kwak, K. Vignesh, N.-K. Park, H.-J. Ryu, J.-I. Baek, M. Kang, Methane formation from photoreduction of CO<sub>2</sub> with water using TiO<sub>2</sub> including Ni ingredient, *Fuel* 143 (2015) 570–576.
- [24] M. Lashgari, S. Soodi, P. Zeinalkhani, Photocatalytic back-conversion of CO<sub>2</sub> into oxygenate fuels using an efficient ZnO/CuO/carbon nanotube solar-energy-material: artificial photosynthesis, *J. CO<sub>2</sub> Util.* 18 (2017) 89–97.
- [25] B.R. Chen, V.H. Nguyen, J.C. Wu, R. Martin, K. Koci, Production of renewable fuels by the photohydrogenation of CO<sub>2</sub>: effect of the Cu species loaded onto TiO<sub>2</sub> photocatalysts, *Phys. Chem. Chem. Phys.* 18 (2016) 4942–4951.
- [26] D.O. Adekoya, M. Tahir, N.A.S. Amin, g-C<sub>3</sub>N<sub>4</sub>/[Cu/TiO<sub>2</sub>] nanocomposite for enhanced photoreduction of CO<sub>2</sub> to CH<sub>3</sub>OH and HCOOH under UV/visible light, *J. CO<sub>2</sub> Util.* 18 (2017) 261–274.
- [27] K. Li, T. Peng, Z. Ying, S. Song, J. Zhang, Ag-loading on brookite TiO<sub>2</sub> quasi nanocubes with exposed {210} and {001} facets: activity and selectivity of CO<sub>2</sub> photoreduction to CO/CH<sub>4</sub>, *Appl. Catal. B: Environ.* 180 (2016) 130–138.
- [28] M. Tahir, N.A.S. Amin, Photo-induced CO<sub>2</sub> reduction by hydrogen for selective CO evolution in a dynamic monolith photoreactor loaded with Ag-modified TiO<sub>2</sub> nanocatalyst, *Int. J. Hydrogen Energy* 42 (2017) 15507–15522.
- [29] B. Tahir, M. Tahir, N.S. Amin, Gold–indium modified TiO<sub>2</sub> nanocatalysts for photocatalytic CO<sub>2</sub> reduction with H<sub>2</sub> as reductant in a monolith photoreactor, *Appl. Surf. Sci.* 338 (2015) 1–14.
- [30] M. Tahir, B. Tahir, N.A.S. Amin, Gold-nanoparticle-modified TiO<sub>2</sub> nanowires for plasmon-enhanced photocatalytic CO<sub>2</sub> reduction with H<sub>2</sub> under visible light irradiation, *Appl. Surf. Sci.* 356 (2015) 1289–1299.
- [31] E. Liu, L. Qi, J. Bian, Y. Chen, X. Hu, J. Fan, H. Liu, C. Zhu, Q. Wang, A facile strategy to fabricate plasmonic Cu modified TiO<sub>2</sub> nano-flower films for photocatalytic reduction of CO<sub>2</sub> to methanol, *Mater. Res. Bull.* 68 (2015) 203–209.
- [32] M. Abou Asi, L. Zhu, C. He, V.K. Sharma, D. Shu, S. Li, J. Yang, Y. Xiong, Visible-light-harvesting reduction of CO<sub>2</sub> to chemical fuels with plasmonic Ag@AgBr/CNT nanocomposites, *Catal. Today* 216 (2013) 268–275.
- [33] M. Tahir, B. Tahir, N.A.S. Amin, Z.Y. Zakaria, Photo-induced reduction of CO<sub>2</sub> to CO with hydrogen over plasmonic Ag-NPs/TiO<sub>2</sub> NWs core/shell hetero-junction under UV and visible light, *J. CO<sub>2</sub> Util.* 18 (2017) 250–260.
- [34] W. Hou, W.H. Hung, P. Pavaskar, A. Goepert, M. Aykol, S.B. Cronin, Photocatalytic conversion of CO<sub>2</sub> to hydrocarbon fuels via plasmon-enhanced absorption and metallic interband transitions, *ACS Catal.* 1 (2011) 929–936.
- [35] A. Gołbińska, A. Malankowska, M. Jarek, W. Lisowski, G. Nowaczyk, S. Jurga, A. Zaleska-Medynska, The effect of gold shape and size on the properties and visible light-induced photoactivity of Au-TiO<sub>2</sub>, *Appl. Catal. B: Environ.* 196 (2016) 27–40.
- [36] V. Jovic, W.-T. Chen, D. Sun-Waterhouse, M.G. Blackford, H. Idriss, G.I.N. Waterhouse, Effect of gold loading and TiO<sub>2</sub> support composition on the activity of Au/TiO<sub>2</sub> photocatalysts for H<sub>2</sub> production from ethanol–water mixtures, *J. Catal.* 305 (2013) 307–317.
- [37] M. Tahir, B. Tahir, N.A.S. Amin, Synergistic effect in plasmonic Au/Ag alloy NPs co-coated TiO<sub>2</sub> NWs toward visible-light enhanced CO<sub>2</sub> photoreduction to fuels, *Appl. Catal. B: Environ.* 204 (2017) 548–560.

- [38] C. Wang, D. Astruc, Nanogold plasmonic photocatalysis for organic synthesis and clean energy conversion, *Chem. Soc. Rev.* 43 (2014) 7188–7216.
- [39] J. Ding, Y. Bu, M. Ou, Y. Yu, Q. Zhong, M. Fan, Facile decoration of carbon fibers with Ag nanoparticles for adsorption and photocatalytic reduction of CO<sub>2</sub>, *Appl. Catal. B: Environ.* 202 (2017) 314–325.
- [40] S. Qin, F. Xin, Y. Liu, X. Yin, W. Ma, Photocatalytic reduction of CO<sub>2</sub> in methanol to methyl formate over CuO-TiO<sub>2</sub> composite catalysts, *J. Colloid Interface Sci.* 356 (2011) 257–261.
- [41] J. Chen, F. Xin, S. Qin, X. Yin, Photocatalytically reducing CO<sub>2</sub> to methyl formate in methanol over ZnS and Ni-doped ZnS photocatalysts, *Chem. Eng. J.* 230 (2013) 506–512.
- [42] O. Ola, M. Maroto-Valer, D. Liu, S. Mackintosh, C.-W. Lee, J.C.S. Wu, Performance comparison of CO<sub>2</sub> conversion in slurry and monolith photoreactors using Pd and Rh-TiO<sub>2</sub> catalyst under ultraviolet irradiation, *Appl. Catal. B: Environ.* 126 (2012) 172–179.
- [43] E. Taboada, I. Angurell, J. Llorca, Dynamic photocatalytic hydrogen production from ethanol–water mixtures in an optical fiber honeycomb reactor loaded with Au/TiO<sub>2</sub>, *J. Catal.* 309 (2014) 460–467.
- [44] T. Wang, L. Yang, X. Du, Y. Yang, Numerical investigation on CO<sub>2</sub> photocatalytic reduction in optical fiber monolith reactor, *Energy Convers. Manage.* 65 (2013) 299–307.
- [45] K. Yuan, L. Yang, X. Du, Y. Yang, Performance analysis of photocatalytic CO<sub>2</sub> reduction in optical fiber monolith reactor with multiple inverse lights, *Energy Convers. Manage.* 81 (2014) 98–105.
- [46] M. Tahir, B. Tahir, Dynamic photocatalytic reduction of CO<sub>2</sub> to CO in a honeycomb monolith reactor loaded with Cu and N doped TiO<sub>2</sub> nanocatalysts, *Appl. Surf. Sci.* 377 (2016) 244–252.
- [47] O. Ola, M.M. Maroto-Valer, Synthesis, characterization and visible light photocatalytic activity of metal based TiO<sub>2</sub> monoliths for CO<sub>2</sub> reduction, *Chem. Eng. J.* 283 (2016) 1244–1253.
- [48] M. Tahir, B. Tahir, N.A. Saidina Amin, H. Alias, Selective photocatalytic reduction of CO<sub>2</sub> by H<sub>2</sub>O/H<sub>2</sub> to CH<sub>4</sub> and CH<sub>3</sub>OH over Cu-promoted In<sub>2</sub>O<sub>3</sub>/TiO<sub>2</sub> nanocatalyst, *Appl. Surf. Sci.* 389 (2016) 46–55.
- [49] S.P. Lim, A. Pandikumar, N.M. Huang, H.N. Lim, Enhanced photovoltaic performance of silver@titania plasmonic photoanode in dye-sensitized solar cells, *RSC Adv.* 4 (2014) 38111–38118.
- [50] A.L. Luna, E. Novoseltceva, E. Louarn, P. Beaunier, E. Kowalska, B. Ohtani, M.A. Valenzuela, H. Remita, C. Colbeau-Justin, Synergetic effect of Ni and Au nanoparticles synthesized on titania particles for efficient photocatalytic hydrogen production, *Appl. Catal. B: Environ.* 191 (2016) 18–28.
- [51] M. Tahir, B. Tahir, N.A.S. Amin, Gold-nanoparticle-modified TiO<sub>2</sub> nanowires for plasmon-enhanced photocatalytic CO<sub>2</sub> reduction with H<sub>2</sub> under visible light irradiation, *Appl. Surf. Sci.* 356 (2015) 1289–1299.
- [52] V. Vaiano, G. Iervolino, D. Sammino, J.J. Murcia, M.C. Hidalgo, P. Ciambelli, J.A. Navio, Photocatalytic removal of patent blue V dye on Au-TiO<sub>2</sub> and Pt-TiO<sub>2</sub> catalysts, *Appl. Catal. B: Environ.* 188 (2016) 134–146.
- [53] S. Bera, J.E. Lee, S.B. Rawal, W.I. Lee, Size-dependent plasmonic effects of Au and Au@SiO<sub>2</sub> nanoparticles in photocatalytic CO<sub>2</sub> conversion reaction of Pt/TiO<sub>2</sub>, *Appl. Catal. B: Environ.* 199 (2016) 55–63.
- [54] T. Okuno, G. Kawamura, H. Muto, A. Matsuda, Photocatalytic properties of Au-deposited mesoporous SiO<sub>2</sub>–TiO<sub>2</sub> photocatalyst under simultaneous irradiation of UV and visible light, *J. Solid State Chem.* 235 (2016) 132–138.
- [55] B. Mei, A. Pougin, J. Strunk, Influence of photodeposited gold nanoparticles on the photocatalytic activity of titanate species in the reduction of CO<sub>2</sub> to hydrocarbons, *J. Catal.* 306 (2013) 184–189.
- [56] M. Murdoch, G.I. Waterhouse, M.A. Nadeem, J.B. Metson, M.A. Keane, R.F. Howe, J. Llorca, H. Idriss, The effect of gold loading and particle size on photocatalytic hydrogen production from ethanol over Au/TiO<sub>2</sub> nanoparticles, *Nat. Chem.* 3 (2011) 489–492.
- [57] Y. Fu, T. Huang, B. Jia, J. Zhu, X. Wang, Reduction of nitrophenols to aminophenols under concerted catalysis by Au/g-C<sub>3</sub>N<sub>4</sub> contact system, *Appl. Catal. B: Environ.* 202 (2017) 430–437.
- [58] M. Tahir, N.S. Amin, Photocatalytic CO<sub>2</sub> reduction with H<sub>2</sub> as reductant over copper and indium co-doped TiO<sub>2</sub> nanocatalysts in a monolith photoreactor, *Appl. Catal. A: Gen.* 493 (2015) 90–102.
- [59] R.A. Rather, S. Singh, B. Pal, A C<sub>3</sub>N<sub>4</sub> surface passivated highly photoactive Au-TiO<sub>2</sub> tubular nanostructure for the efficient H<sub>2</sub> production from water under sunlight irradiation, *Appl. Catal. B: Environ.* 213 (2017) 9–17.
- [60] M. Kim, Y.K. Kim, S.K. Lim, S. Kim, S.-I. In, Efficient visible light-induced H<sub>2</sub> production by Au@CdS/TiO<sub>2</sub> nanofibers: synergistic effect of core–shell structured Au@CdS and densely packed TiO<sub>2</sub> nanoparticles, *Appl. Catal. B: Environ.* 166–167 (2015) 423–431.